



Proper evaluation of spherical harmonics-based expressions for the velocity and vortex stretching vectors in three-dimensional grid-free vortex methods

Samer Salloum, Issam Lakkis*

Department of Mechanical Engineering, American University of Beirut, Beirut, Lebanon

ARTICLE INFO

Article history:

Received 18 July 2019

Received in revised form 27 March 2020

Accepted 24 May 2020

Available online 1 June 2020

Keywords:

Three dimensional vortex methods

Grid-free

Fast multipoles

Collision of two vortex rings

Redistribution Scheme

ABSTRACT

We present expressions for approximating the velocity and vortex stretching vectors induced by a far-field collection of point vortices and we propose a set of recurrence relations to properly evaluate these expressions. Expressed as truncated series of spherical harmonics, these approximations are used in the context of $\mathcal{O}(N \log N)$ and $\mathcal{O}(N)$ -type fast multipole methods to reduce the computational cost of the advection step in three-dimensional grid-free vortex methods. These methods typically rely on operator splitting to handle diffusion and convection separately. In our implementation, the convection step employs a second order Runge-Kutta time integration scheme, where the particles velocities and vortex stretching vectors are computed using a fast multipole method that employs the proposed expressions. To model diffusion, we introduce an extension of the smoothed redistribution scheme to 3D unbounded flows. We check the accuracy of the expressions by inspecting the convergence of the velocity and the vortex stretching vectors as a function of the expansion order. The performance of the grid-free three-dimensional vortex method is assessed by simulating the collision of two vortex rings, over a long period of time, for different values of Reynolds number covering the range 500 – 2000.

© 2020 Elsevier Inc. All rights reserved.

1. Introduction

Vortex methods [1–4] are Lagrangian mesh-free methods for numerically solving the vorticity equation. They were originally based on Helmholtz's circulation theorem which states that, in a barotropic inviscid fluid subject to conservative body forces, the circulation is conserved along particles trajectories. Under these conditions, a complete description of the flow field is obtained by tracking the motion of vorticity-carrying fluid elements [4], starting with an initial vorticity distribution. In these methods, the vorticity field is discretized using singular or regularized vortex blobs. Operator splitting is used to numerically solve the vorticity equation in two separate steps. The convection step commonly employs a high order Runge-Kutta time integration scheme, where the particles are advected with the local velocity field, and their vorticity strengths are adjusted to account for straining of the vorticity vector by the local velocity gradient field. The velocity and the vortex stretching vectors at particles locations are computed using a Biot-Savart type summation over all the particles. In the diffusion step, the vorticity strengths of the particles are modified to account for viscous effects.

* Corresponding author.

E-mail addresses: sos07@aub.edu.lb (S. Salloum), ilakkis@alum.mit.edu (I. Lakkis).

As the number of elements is increased, regularized vortex methods converge to the exact solution provided that the core overlapping condition is maintained and that particle remeshing is done every few time steps [5]. Without particle remeshing, Lagrangian methods rapidly lose their accuracy especially in high inertia flows where large strain rates cause the particles to move away from each other thereby violating the overlap condition. Particle remeshing usually employs the M'_4 high order interpolation scheme which preserves the total circulation, linear and angular impulses. However, this interpolation scheme introduces some dissipation [6], effectively acting as a hyper-viscosity.

Since their inception, vortex methods underwent tremendous progress. The first vortex simulations were conducted by Rosenhead [7] using 12 point vortices in two dimensions. Birkhof and Fisher [8] showed that the vortices must be regularized to satisfactorily approximate a vortex sheet. Many of the aspects of modern vortex methods are due to the pioneering work of Chorin [9], who introduced the notion of vortex blob and repeated the work of Rosenhead by using regularized vortex cores. Chorin also introduced the random-walk method for grid-free modeling of diffusion in slightly viscous two-dimensional flows. The advent of grid-free diffusion modeling methods [10,2,11–13], along with the development of $\mathcal{O}(N \log N)$ and $\mathcal{O}(N)$ fast solvers for fast computation of the velocity and vortex stretching vectors [14,15] and the proper handling of different boundary conditions [16,17] and of source terms [18,19] made vortex methods potentially a viable alternative to grid-based methods for numerically solving the Navier-Stokes equations at a high resolution [4]. Vortex methods have been utilized extensively in simulating inviscid and high inertia flows including vortex sheets [20,21], unsteady separated flows [22–24], high Reynolds number wakes [25], and various three-dimensional problems involving vortex rings, jets, and wakes [26–28]. They have also been used to study reacting shear layers [29,30], Rayleigh Taylor flows [31], fire plumes [32,33], diffusion-controlled combustion [13], and unsteady two-dimensional compressible flows [34]. These methods were also employed for simulating buoyant flows [35,19], reacting flows [36,37], radiation in participating media [38], and reacting-radiating flows [39].

When compared to grid-based methods, grid-free vortex methods possess several desirable features that kept them of continuous interest. In addition to being completely mesh-free, vortex methods are highly adaptive because only regions of non-vanishing vorticity are represented the computational elements [40]. Furthermore, since these elements are advected by the velocity field, there is no need for explicit numerical discretization of the convection term, which is a common source of numerical diffusion in grid-based methods. These methods, by virtue of their Lagrangian nature, demonstrated exceptional ability to capture the small scale features in high inertia flows. Another advantage is that the continuity equation is automatically satisfied for incompressible fluids since the velocity field is computed as the curl of a vector potential. The absence of the pressure term in the vorticity equation is another attractive feature [3]. Moreover, the satisfactory energy conservation properties of vortex methods, in addition to their small dispersion error, made them suitable to simulate convection-dominated problems [6]. However, and although it was reported in [41] that vortex methods can be faster than Eulerian finite-difference methods due to the increased stability and larger time steps, vortex methods had not yet reached a level of maturity where they can be considered as an efficient alternative to Eulerian methods. This is because vortex methods still face some major challenges, especially the challenge of maintaining a divergence free vorticity field without affecting the conserved quantities. In fact, although the divergence of the initial vorticity can be made small enough by using a sufficiently large number of elements, maintaining the divergence free condition of the vorticity field remains without any doubt the weakest point of the 3D vortex particle method [42]. According to Winckelmans [5], the vorticity divergence is naturally damped by viscous diffusion especially when the simulation is well-resolved and particle remeshing is used. However, for long time simulations, enforcing the divergence free condition is essential especially in high inertia flows. To this end, Winckelmans [43] proposed the W-scheme and reported, upon examining this scheme in addition to the P-scheme [44], that both schemes are diffusive.

The accurate calculation of the velocity and vortex stretching vectors is crucial in vortex methods. In fact, the velocity is used to advect vortex elements using a time step that is typically larger than that used in Eulerian methods. Thus, advecting with an inaccurate velocity over a large time step will introduce errors in the particles trajectories resulting in an inaccurate vorticity field over short times. Moreover, since the vortex stretching vector, expressed as the dot product of the vorticity vector and the rate of strain tensor, is used to update the vorticity using the Helmholtz equation, inaccurate computation of the rate of strain tensor over a large time step will introduce time integration errors in the vorticity representation and will eventually impact the flow invariants such as total circulation, linear impulse, and angular impulse. Although it is essential to accurately compute the velocity and its spatial derivatives, calculating these terms through direct summation comes at a prohibitive $\mathcal{O}(N^2)$ cost, especially for simulating three dimensional flows, where a large N is needed to capture the small scale features. This challenge has been alleviated by the advent of fast methods for the N body problems [14,15,45].

Traditionally, two variants of fast methods for approximating the Biot-Savart summation are found in the literature. They are the vortex in cell methods (VIC) [45] and the hierarchical N -body fast multipoles solver [14,15]. The vortex in cell methods (VIC) are tailored for computing the velocity and vortex stretching on a grid [46]. In fact, the vorticity is first interpolated on a grid and the vector potential is calculated on this grid using a Poisson solver based on the Fast Fourier Transform. The velocity and vortex stretching are then calculated by centered finite difference on the grid and then interpolated back to the particle locations. The particles are then advected using the velocities at their locations and the vorticity strengths are adjusted to account for vortex stretching. VIC method still has negligible dispersion error since the particles are advected in a Lagrangian way. Moreover, the divergence free condition of the vorticity field is maintained by projecting the vorticity field onto a divergence free basis. This operation provides an efficient and essentially non-diffusive “relaxation” scheme, which allows for simulations at high Reynolds number and for arbitrarily long times [5].

Although VIC methods are very fast and relatively simple to implement, they face the challenge of setting up the proper boundary conditions of the Poisson solver in unbounded or semi-bounded domains. The grid must be taken much larger than the vorticity field region to provide approximate analytical boundary conditions for the vector potential, $\vec{\psi}$. To this end, Chatelain and Koumoutsakos [47] presented a computationally efficient, adaptive solver for the solution of the Poisson and Helmholtz equation in domains with combinations of unbounded and periodic directions. The method relies on FFTs in all directions and doubles the domain size in the non-periodic directions.

Alternatively, hierarchical N -body fast solvers are flexible and preserve the grid-free nature of vortex methods. The following two variants of these methods have been developed, treecodes [14] and FMMs [48]. Compared to the direct summation, which has a complexity of $O(N^2)$, the treecode algorithm [14] achieves a complexity of $O(N \log N)$. It does so by clustering source particles into larger bins within a recursive tree-based division operation and using multipole expansions to approximate their influence on the targets. In this context, Salmon and Warren [49] formulated multipole moments expressions for an arbitrary Green's function by performing Taylor expansion and developed simple expressions for the upper bounds error for the potential field and its gradient. The fast multipole method (FMM) [15] extends the Barnes-Hut treecode [14] by including local expansions to further reduce the computational cost. By clustering the nearby target particles [50], in addition to the source particles, the FMM [15] can achieve $O(N)$ complexity. Implementation of FMM on de-singularized particles increases the cost to $O(N^{1.2})$ [43]. A combination of vortex-in-cell (VIC) and parallel fast multipole methods (FMM) to simulate unbounded and half-bounded incompressible unsteady flows is presented in [6]. The exact Dirichlet boundary conditions for $\vec{\psi}$ are obtained using the parallel fast multipole (FMM) method. These boundary conditions are used to solve the Poisson equation on a grid without the need of expanding the grid dimension.

FMMs have therefore become an essential component of vortex methods. Yet, little effort has been devoted to formulate compact expressions of the velocity and vortex stretching vectors as a truncated series of spherical harmonics. Winkel-mans [43], Ploumhans [51], and Cocle [6], among others used analytical derivatives of the multipole expansions to evaluate the velocity vector and the velocity gradient. Yokota [52–54] described the expressions for both the velocity and stretching vectors in several of his papers but he didn't discuss how to deal with the spatial derivatives of spherical harmonics. Berdowski (2016) [55] presented a detailed derivation for approximating the velocity and stretching vectors using multipole expansions and implemented them in $O(N \log N)$ fast multipole algorithm. The discussion, however, does not include local expansions since they are not needed in the $O(N \log N)$ -type fast solver. Furthermore, evaluating the velocity and vortex stretching vectors using the equations presented in [55] requires dividing by $\sin\theta$ and $\sin^2\theta$, where direct numerical evaluation is problematic as the polar angle θ approaches zero at the poles.

In this paper we present simple alternative expressions for the velocity and vortex stretching vectors using both local and multipole expansion coefficients, and we propose a set of recurrence relations to properly evaluate these expressions over the entire range of the polar angle. We use these expressions in simulating the advection-diffusion problem of the collision of two vortex rings, over a long period of time, for the following values of Reynolds number: 500, 1000, 1500, 2000. The method used is completely grid-free and the operator splitting scheme employs a second Runge-Kutta time integration step for advection. The method also employs a novel extension to three-dimensions of the redistribution method for the diffusion step.

2. Vortex methods and the vorticity transport equation

For three dimensional incompressible flow, $\nabla \cdot \vec{u} = 0$, the evolution of the vorticity, $\vec{\omega}$, is described by the Helmholtz's vorticity equation:

$$\frac{d\vec{\omega}}{dt} = (\vec{\omega} \cdot \nabla) \vec{u} + \frac{\nabla \rho \times \nabla p}{\rho} + \nabla^2 \vec{\omega} \quad (1)$$

where t is time, \vec{u} is the velocity, ρ is the density, p is the pressure, and d/dt is the Lagrangian derivative $d/dt = \partial/\partial t + \vec{u} \cdot \nabla$.

For an incompressible flow in unbounded domain, the velocity vector field is computed as the curl of a vector potential field $\vec{\psi}$

$$\vec{u} = \nabla \times \vec{\psi} \quad (2)$$

Noting that the vorticity vector field is the curl of the velocity vector field

$$\vec{\omega} = \nabla \times \vec{u} = \nabla \times (\nabla \times \vec{\psi}), \quad (3)$$

$\vec{\psi}$ solves the Poisson equation

$$\nabla^2 \vec{\psi} = -\vec{\omega} \quad (4)$$

The Green's function for the Poisson equation (4) in an unbounded domain is $G(\vec{x}) = -\frac{1}{4\pi\|\vec{x}\|}$, so that

$$\vec{\psi}(\vec{x}, t) = \frac{1}{4\pi} \int \frac{\vec{\omega}(\vec{y}, t)}{\|\vec{x} - \vec{y}\|} d^3y \quad (5)$$

In vortex methods, the vorticity field is discretized using vortex elements. The elements can be point vortices (singular representation of the vorticity field) or blobs (regularized representation of the vorticity field). Associated with each element i are the position vector \vec{x}_i and the strength vector $\vec{\alpha}_i$. Assuming a singular representation of the vorticity field,

$$\vec{\omega}_\delta(\vec{x}, t) = \sum_{i=1}^N \vec{\alpha}_i \delta(\vec{x} - \vec{x}_i), \quad (6)$$

where N is the number of elements and δ is the Dirac delta function, the vector potential field and the velocity vector field can be approximated as

$$\vec{\psi}_\delta(\vec{x}, t) = \frac{1}{4\pi} \sum_{i=1}^N \frac{\vec{\alpha}_i(t)}{\|\vec{x}(t) - \vec{x}_i(t)\|} \quad (7)$$

$$\vec{u}_\delta(\vec{x}, t) = \nabla \times \vec{\psi}_\delta = -\frac{1}{4\pi} \sum_{i=1}^N \frac{(\vec{x}(t) - \vec{x}_i(t))}{\|\vec{x}(t) - \vec{x}_i(t)\|^3} \times \vec{\alpha}_i(t) \quad (8)$$

A regularized representation of the vorticity field may be expressed as

$$\vec{\omega}_\sigma(\vec{x}, t) = \sum_{i=1}^N \vec{\alpha}_i(t) \zeta_\sigma(\vec{x} - \vec{x}_i), \quad (9)$$

where ζ_σ is a regularization function and σ is the associated smoothing radius. The regularization function is usually taken as a radially symmetric function, $\zeta_\sigma(\vec{x} - \vec{x}_i) = \frac{1}{\sigma^3} \zeta\left(\frac{\|\vec{x} - \vec{x}_i\|}{\sigma}\right) = \frac{1}{\sigma^3} \zeta\left(\frac{r}{\sigma}\right)$, that satisfies the normalization condition

$$4\pi \int_0^\infty \zeta_\sigma(\rho) \rho^2 d\rho = 1. \quad (10)$$

A regularization function of order l , that conserves up to order $l - 1$ moments as the Dirac function, can be constructed as described in [56]. Using a radially symmetric regularization function, the corresponding vector potential field and the velocity vector field can be approximated as

$$\vec{\psi}_\sigma(\vec{x}, t) = \sum_{i=1}^N G_\sigma(\vec{x} - \vec{x}_i) \vec{\alpha}_i(t) \quad (11)$$

$$\vec{u}_\sigma(\vec{x}, t) = \nabla \times \vec{\psi}_\sigma = -\sum_{i=1}^N q_\sigma(\vec{x}(t) - \vec{x}_i(t)) \frac{(\vec{x}(t) - \vec{x}_i(t))}{\|\vec{x}(t) - \vec{x}_i(t)\|^3} \times \vec{\alpha}_i(t) \quad (12)$$

Where G solves the Poisson equation $\nabla^2 G = -\zeta(r)$, $G_\sigma(r) = \frac{1}{\sigma} G\left(\frac{r}{\sigma}\right)$, $q(r) = \int_0^r \zeta(\rho) \rho^2 d\rho$, and $q_\sigma(r) = q\left(\frac{r}{\sigma}\right)$ [57].

Direct evaluation of the velocity vector and the rate of strain tensor requires $O(N^2)$ computational operations of all the pairwise interaction in a system of N particles. The high cost of direct evaluation severely compromises the viability of the method to simulate transient flows, especially for cases where the number of particles, required to accurately resolve the vorticity field, grows considerably with time. Alternatively, the fast multipole method (FMM) enables conducting these simulations with a reasonable cost. Next, we briefly present the $O(N \log N)$ and $O(N)$ fast solvers.

3. The fast multipole in three dimensions

The $O(N \log N)$ fast multipole scheme is based on approximating, to an arbitrary precision, the vector potential induced by clusters of singular vortices in the far field using multipole expansions [58]. Implementation of $O(N)$ scheme requires, in addition, the use of local expansions to further reduce the order of the computations. These two expansions are based on spherical harmonics, $Y_n^m(\theta, \varphi)$, $n \in \mathbb{N}$, $|m| \leq n$, which form a frequency-space basis for representing functions on a sphere. Thus, any spherical vector field $\vec{\phi}(\theta, \varphi)$ may be expanded as the linear combination $\vec{\phi}(\theta, \varphi) = \sum_{n=0}^\infty \sum_{m=-n}^{m=n} \vec{C}_n^m Y_n^m(\theta, \varphi)$, where the coefficients \vec{C}_n^m are computed by projecting $\vec{\phi}$ onto each basis function Y_n^m .

We note that for a regularized representation of the vorticity field, these same expansions (which are based on point vortices) are used to calculate the effect of the far field. In this case, the use of multipole expansion coefficients to approximate the far-field vector potential $\vec{\psi}_\sigma$ will induce an error that is made up of the following two components:

1. A component resulting from truncating multipole expansions at some order p : This error is related to the series expansion used to represent the kernel $\frac{1}{r}$ at large distance and is a function of the order of expansion p and the Multipole Acceptance Criteria. This error decreases exponentially as p increases and converges to zero as $p \rightarrow \infty$.

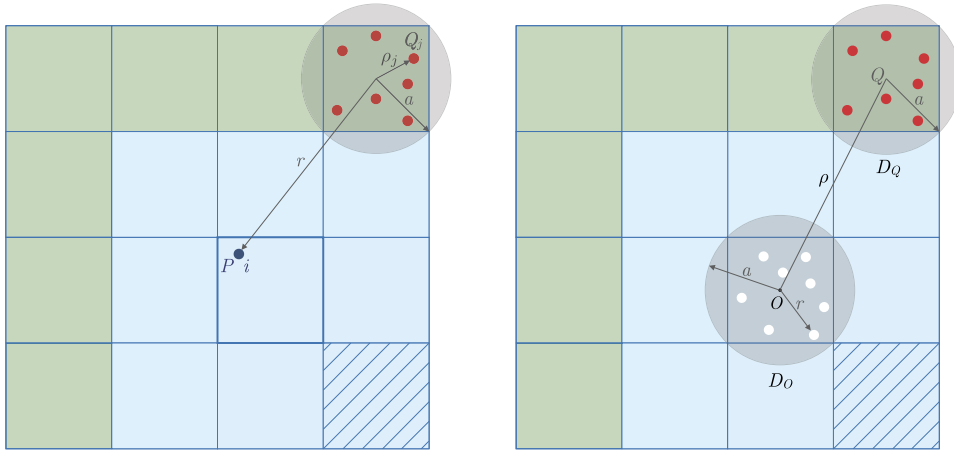


Fig. 1. Schematic for the $\mathcal{O}(N \log N)$ (left) and $\mathcal{O}(N)$ (right) FM schemes.

2. A component resulting from approximating the Biot-Savart kernel by a $\frac{1}{r}$ kernel: This error arises due to the fact that G_σ deviates from $\frac{1}{4\pi r}$. This error mainly depends on the size of the smallest boxes (at the deepest level of the tree). In order to neglect this error, we must keep the leaf boxes width above a minimum multiple of the core function smoothing radius. In three dimensional flows, this will pose a considerable computational overload on the FM schemes, since it will dramatically increase the particle to particle interaction.

3.1. Multipole expansion of the vector potential field

Suppose that s vortices having strengths $(\vec{\alpha}_j, j = 1 \dots s)$ are located at the points $\vec{Q}_j = (\rho_j, \theta_j, \varphi_j)$ inside the sphere D_Q , with $|\rho_j| < a$ (see Fig. 1, left), then at any $\vec{P} = (r, \theta, \varphi)$ with $r > a$, the vector potential field is given by

$$\vec{\psi}_\delta(\vec{P}, t) = \frac{1}{4\pi} \sum_{n=0}^{\infty} \sum_{m=-n}^n \frac{\vec{M}_n^m}{r^{n+1}} Y_n^m(\theta, \varphi) \quad (13)$$

with

$$\vec{M}_n^m = \sum_{j=1}^s \vec{\alpha}_j \rho_j^n Y_n^{-m}(\theta_j, \varphi_j) \quad (14)$$

Furthermore, for any $p \geq 1$

$$\left\| \vec{\psi}_\delta(\vec{P}, t) - \frac{1}{4\pi} \sum_{n=0}^p \sum_{m=-n}^n \frac{\vec{M}_n^m}{r^{n+1}} Y_n^m(\theta, \varphi) \right\| \leq \frac{1}{4\pi} \frac{\Gamma_{D_Q}}{r-a} \left(\frac{a}{r}\right)^{p+1} \quad (15)$$

where

$$\Gamma_{D_Q} = \sum_{j=1}^s \|\vec{\Gamma}_j\| \quad (16)$$

Thus, at a given point $P = (r, \theta, \varphi)$ with $r > a$, the vector potential is approximated by

$$\vec{\psi}_\delta(\vec{P}, t) \simeq \frac{1}{4\pi} \sum_{n=0}^p \sum_{m=-n}^n \frac{\vec{M}_n^m}{r^{n+1}} Y_n^m(\theta, \varphi) \quad (17)$$

3.2. Local expansion of the vector potential field

Suppose that s vortices having strengths $(\vec{\alpha}_j, j = 1 \dots s)$ are located inside the sphere D_Q of radius a with center at $Q = (\rho, \alpha, \beta)$ (see Fig. 1, right), and that $\rho = (c+1)a$ with $c > 1$, then for any point $P(r, \theta, \phi)$ inside D_O of radius a centered at the origin, the vector potential due to vortices $(\vec{\alpha}_j, j = 1 \dots s)$ inside D_Q is described by the following local expansion

$$\vec{\psi}_\delta(P, t) = \frac{1}{4\pi} \sum_{n=0}^{\infty} \sum_{m=-n}^n \vec{L}_n^m Y_n^m(\theta, \varphi) r^n, \quad (18)$$

where

$$\vec{L}_n^m = \sum_{j=0}^{\infty} \sum_{k=-j}^j \frac{\vec{M}_j^k i^{|m-k|-|m|-|k|} A_j^k A_n^m \cdot \rho^j \cdot Y_{n+j}^{k-m}(\alpha, \beta)}{(-1)^j A_{n+j}^{k-m} \cdot \rho^{n+j+1}}, \quad (19)$$

with A_n^m defined by

$$A_n^m = \frac{(-1)^n}{\sqrt{(n-m)!(n+m)!}} \quad (20)$$

Furthermore, for any $p \geq 1$,

$$\| \vec{\psi}_\delta(P, t) - \frac{1}{4\pi} \sum_{n=0}^{\infty} \sum_{m=-n}^n \vec{L}_n^m Y_n^m(\theta, \varphi) r^n \| \leq \frac{\Gamma_{D_Q}}{a(c-1)} \left(\frac{1}{c} \right)^{p+1} \quad (21)$$

Thus, at a given point $P = (r, \theta, \varphi)$ with $r < a$, the vector potential due to vortices inside D_Q is approximated by

$$\vec{\psi}_\delta(P, t) = \frac{1}{4\pi} \sum_{n=0}^p \sum_{m=-n}^n \vec{L}_n^m Y_n^m(\theta, \varphi) r^n \quad (22)$$

The spherical harmonics can be expressed in term of the associated Legendre polynomials [15] as

$$Y_n^m(\theta, \varphi) = \sqrt{\frac{(n-|m|)!}{(n+|m|)!}} P_n^{|m|}(\cos \theta) e^{im\varphi} \quad (23)$$

There are many ways to define the associated Legendre polynomials P_n^m and its derivatives [59]. We propose next a set of recurrence relations to properly evaluate these polynomials and their first and second order derivatives over the entire range of polar angle.

4. Alternative simple expressions for the velocity and vortex stretching vectors expressed as a truncated series of spherical harmonics

In three-dimensional vortex methods, computing the velocity and the vortex stretching vectors at the particles positions is required every time step. Expressions for the far-field component of these two vectors in term of spherical harmonics can be obtained respectively from the corresponding spatial derivatives of the vector potential approximations in Eqs. (17) and (22), as presented below. These expressions are used in the context of $\mathcal{O}(N \log N)$ and $\mathcal{O}(N)$ FM schemes to reduce the computational cost of the advection step.

4.1. Expressions for the velocity vector in term of multipole and local expansion coefficients

The velocity vector \vec{u}_δ is computed as the curl of the vector potential $\vec{\psi}_\delta$. Expanding $\vec{\psi}_\delta$ in term of multipole expansion coefficients \vec{M}_n^m using Eq. (17), and taking the curl of $\vec{\psi}_\delta$, the velocity vector can be expressed as

$$\vec{u}_\delta = \frac{1}{4\pi} \sum_{n=0}^p \sum_{m=-n}^n \nabla \left(\frac{Y_n^m(\theta, \varphi)}{r^{n+1}} \right) \times \vec{M}_n^m \quad (24)$$

In Cartesian coordinates, we get

$$\vec{u}_\delta = \frac{1}{4\pi} \sum_{n=1}^p \sum_{m=-n}^n \frac{C_n^m e^{im\varphi}}{r^{n+2}} \begin{pmatrix} \sin \theta \cos \varphi & \cos \theta \cos \varphi & -\sin \varphi \\ \sin \theta \sin \varphi & \cos \theta \sin \varphi & \cos \varphi \\ \cos \theta & -\sin \theta & 0 \end{pmatrix} \begin{pmatrix} -(n+1)P_n^m \\ \frac{dP_n^m}{d\theta} \\ \frac{imP_n^m}{\sin \theta} \end{pmatrix} \times \vec{M}_n^m, \quad (25)$$

where

$$C_n^m = \sqrt{\frac{(n-|m|)!}{(n+|m|)!}} \quad (26)$$

Expanding $\vec{\psi}_\delta$ in term of local expansion coefficients \vec{L}_n^m using equation (18), the velocity vector can be expressed as

$$\vec{u}_\delta = \nabla \times \vec{\psi}_\delta(P, t) = \frac{1}{4\pi} \sum_{n=0}^p \sum_{m=-n}^n \nabla(r^n Y_n^m(\theta, \varphi)) \times \vec{L}_n^m \quad (27)$$

In cartesian coordinates, we get

$$\vec{u}_\delta = \frac{1}{4\pi} \sum_{n=1}^p \sum_{m=-n}^n r^{n-1} C_n^m e^{im\varphi} \begin{pmatrix} \sin \theta \cos \varphi & \cos \theta \cos \varphi & -\sin \varphi \\ \sin \theta \sin \varphi & \cos \theta \sin \varphi & \cos \varphi \\ \cos \theta & -\sin \theta & 0 \end{pmatrix} \begin{pmatrix} n P_n^m \\ \frac{dP_n^m}{d\theta} \\ \frac{imP_n^m}{\sin \theta} \end{pmatrix} \times \vec{L}_n^m \quad (28)$$

4.2. Expressions for the vortex stretching vector in term of multipole and local expansion coefficients

The vortex stretching vector, $(\vec{\alpha} \cdot \nabla) \vec{u}_\delta$, quantifies the stretching and tilting of the vorticity due to the flow velocity gradients. It is computed as the projection of the rate of strain tensor (gradient of the velocity vector) along the direction of the vorticity vector $\vec{\omega}$, scaled by the magnitude of the vorticity $||\vec{\omega}||$.

The rate of stain tensor is expressed in Cartesian coordinates as

$$\nabla \vec{u}_\delta = \begin{pmatrix} \frac{\partial u_\delta}{\partial x} & \frac{\partial u_\delta}{\partial y} & \frac{\partial u_\delta}{\partial z} \\ \frac{\partial v_\delta}{\partial x} & \frac{\partial v_\delta}{\partial y} & \frac{\partial v_\delta}{\partial z} \\ \frac{\partial w_\delta}{\partial x} & \frac{\partial w_\delta}{\partial y} & \frac{\partial w_\delta}{\partial z} \end{pmatrix} \quad (29)$$

Thus the rate of stain tensor is determined completely by the three vectors $\frac{\partial \vec{u}_\delta}{\partial x}$, $\frac{\partial \vec{u}_\delta}{\partial y}$, $\frac{\partial \vec{u}_\delta}{\partial z}$, representing the variation of the velocity vector along the x, y, and z directions respectively. Applying the chain rule in partial differentiation we obtain:

$$\begin{pmatrix} \frac{\partial}{\partial x} \\ \frac{\partial}{\partial y} \\ \frac{\partial}{\partial z} \end{pmatrix} \vec{u}_\delta = \begin{pmatrix} \sin \theta \cos \varphi & \cos \theta \cos \varphi & -\sin \varphi \\ \sin \theta \sin \varphi & \cos \theta \sin \varphi & \cos \varphi \\ \cos \theta & -\sin \theta & 0 \end{pmatrix} \begin{pmatrix} \frac{\partial}{\partial r} \\ \frac{1}{r} \frac{\partial}{\partial \theta} \\ \frac{1}{r \sin \theta} \frac{\partial}{\partial \varphi} \end{pmatrix} \vec{u}_\delta \quad (30)$$

Expanding \vec{u}_δ in term of multipole expansion coefficients \vec{M}_n^m using Eq. (25) and differentiating with respect to r, θ , and ϕ , we obtain:

$$\frac{\partial \vec{u}_\delta}{\partial r} = \frac{1}{4\pi} \sum_{n=2}^p \sum_{m=-n}^n \frac{-(n+2)}{r^{n+3}} C_n^m e^{im\varphi} \begin{pmatrix} \sin \theta \cos \varphi & \cos \theta \cos \varphi & -\sin \varphi \\ \sin \theta \sin \varphi & \cos \theta \sin \varphi & \cos \varphi \\ \cos \theta & -\sin \theta & 0 \end{pmatrix} \begin{pmatrix} -(n+1) P_n^m \\ \frac{dP_n^m}{d\theta} \\ \frac{imP_n^m}{\sin \theta} \end{pmatrix} \times \vec{M}_n^m \quad (31)$$

$$\frac{1}{r} \frac{\partial \vec{u}_\delta}{\partial \theta} = \frac{1}{4\pi} \sum_{n=2}^p \sum_{m=-n}^n \frac{1}{r^{n+3}} C_n^m e^{im\varphi} \begin{pmatrix} \sin \theta \cos \varphi & \cos \theta \cos \varphi & -\sin \varphi \\ \sin \theta \sin \varphi & \cos \theta \sin \varphi & \cos \varphi \\ \cos \theta & -\sin \theta & 0 \end{pmatrix} \begin{pmatrix} -(n+2) \frac{dP_n^m}{d\theta} \\ \frac{d^2 P_n^m}{d\theta^2} - (n+1) P_n^m \\ i \frac{d}{d\theta} \left(\frac{mP_n^m}{\sin \theta} \right) \end{pmatrix} \times \vec{M}_n^m \quad (32)$$

$$\frac{1}{r \sin \theta} \frac{\partial \vec{u}_\delta}{\partial \varphi} = \frac{1}{4\pi} \sum_{n=2}^p \sum_{m=-n}^n \frac{1}{r^{n+3}} C_n^m e^{im\varphi} \begin{pmatrix} \sin \varphi D_n^m - im \cos \varphi D_n^m - (m^2 - 1) \frac{P_n^m}{\sin^2 \theta} \\ -\cos \varphi D_n^m - im \sin \varphi D_n^m - (m^2 - 1) \frac{P_n^m}{\sin^2 \theta} \\ -im \left(\frac{dP_n^m}{d\theta} + (n+1) \frac{\cos \theta}{\sin \theta} P_n^m \right) \end{pmatrix} \times \vec{M}_n^m \quad (33)$$

where

$$D_n^m = \frac{d^2 P_n^m}{d\theta^2} + (n+1)^2 P_n^m \quad (34)$$

Expanding \vec{u}_δ in term of local expansion coefficients \vec{L}_n^m using Eq. (28) and differentiating with respect to r, θ , and ϕ , we obtain:

$$\frac{\partial \vec{u}_\delta}{\partial r} = \frac{1}{4\pi} \sum_{n=2}^p \sum_{m=-n}^n (n-1) r^{n-2} C_n^m e^{im\varphi} \begin{pmatrix} \sin \theta \cos \varphi & \cos \theta \cos \varphi & -\sin \varphi \\ \sin \theta \sin \varphi & \cos \theta \sin \varphi & \cos \varphi \\ \cos \theta & -\sin \theta & 0 \end{pmatrix} \begin{pmatrix} n P_n^m \\ \frac{dP_n^m}{d\theta} \\ \frac{imP_n^m}{\sin \theta} \end{pmatrix} \times \vec{L}_n^m \quad (35)$$

$$\frac{1}{r} \frac{\partial \vec{u}_\delta}{\partial \theta} = \frac{1}{4\pi} \sum_{n=2}^p \sum_{m=-n}^n r^{n-2} C_n^m e^{im\varphi} \begin{pmatrix} \sin \theta \cos \varphi & \cos \theta \cos \varphi & -\sin \varphi \\ \sin \theta \sin \varphi & \cos \theta \sin \varphi & \cos \varphi \\ \cos \theta & -\sin \theta & 0 \end{pmatrix} \begin{pmatrix} (n-1) \frac{dP_n^m}{d\theta} \\ \frac{d^2 P_n^m}{d\theta^2} + n P_n^m \\ i \frac{d}{d\theta} \left(\frac{mP_n^m}{\sin \theta} \right) \end{pmatrix} \times \vec{L}_n^m \quad (36)$$

$$\frac{1}{r \sin \theta} \frac{\partial \vec{u}_\delta}{\partial \varphi} = \frac{1}{4\pi} \sum_{n=2}^p \sum_{m=-n}^n r^{n-2} C_n^m e^{im\varphi} \begin{pmatrix} \sin \varphi F_n^m - im \cos \varphi F_n^m - (m^2 - 1) \frac{P_n^m}{\sin^2 \theta} \\ -\cos \varphi F_n^m - im \sin \varphi F_n^m - (m^2 - 1) \frac{P_n^m}{\sin^2 \theta} \\ -im \left(\frac{dP_n^m}{d\theta} - n \frac{\cos \theta}{\sin \theta} P_n^m \right) \end{pmatrix} \times \vec{L}_n^m \quad (37)$$

where

$$F_n^m = \frac{d^2 P_n^m}{d\theta^2} + n^2 P_n^m \quad (38)$$

4.3. Proper evaluation of the velocity and vortex stretching vectors over the entire range of the polar angle

So far, we derived expressions for the velocity and vortex stretching in terms of $(P_n^m, \frac{dP_n^m}{d\theta}, \frac{d^2 P_n^m}{d\theta^2}, \frac{P_n^m}{\sin \theta}, \frac{d}{d\theta} \frac{mP_n^m}{\sin \theta}, \text{ and } \frac{P_n^m}{\sin^2 \theta})$. Direct numerical evaluation of the last three terms yield values that tend to infinity when approaching the poles, owing to the fact that $\sin \theta$ and $\sin^2 \theta$ tend to zero as θ approach zero. Next we present a method, based on recurrence relations, that allows accurate evaluation of these terms over the entire range of the polar angle, θ .

Noting that the associated Legendre polynomial can be written in the form $P_n^m = f(\cos \theta) \sin^m \theta$, we introduce the two functions, $\alpha_n^m = \frac{P_n^m}{\sin^2 \theta}$ for $m \geq 2$ and $\beta_n^m = \frac{P_n^m}{\sin \theta}$ for $m \geq 1$. In Eqs. (25) and (28) of the velocity vector, and in Eqs. (31)–(33) and (35)–(37) of the velocity spatial derivatives, the term $\frac{P_n^m}{\sin \theta}$ is always multiplied by m . So we extend the definition of β_n^m by imposing $\beta_n^0 = 0$. Furthermore, the term $\frac{P_n^m}{\sin^2 \theta}$ is always multiplied by $m(m^2 - 1)$. We also extend the definition of α_n^m by imposing $\alpha_n^0 = \alpha_n^1 = 0$. By introducing these two functions, we have $m(m^2 - 1)\alpha_n^m = m(m^2 - 1)\frac{P_n^m}{\sin^2 \theta}$ and $m\beta_n^m = m\frac{P_n^m}{\sin \theta}$ for any pair (n, m) .

To numerically evaluate these associate Legendre polynomial expressions in a robust manner, we propose an algorithm that uses the following recurrence relations defined for $n > 2$ and $m > 1$.

$$P_n^m = \sin^2 \theta \alpha_n^m \quad (39)$$

$$P_n^1 = \sin \theta \beta_n^1 \quad (40)$$

$$nP_n^0 = (2n - 1) \cos \theta P_{n-1}^0 - (n - 1)P_{n-2}^0 \quad (41)$$

where

$$\alpha_n^n = (-1)^n (2n - 1)!! \sin^{n-2} \theta \quad (42)$$

$$(n - m)\alpha_n^m = (2n - 1) \cos \theta \alpha_{n-1}^m - (n + m - 1)\alpha_{n-2}^m \quad (43)$$

$$\beta_n^m = \sin \theta \alpha_n^m \quad (44)$$

$$(n - 1)\beta_n^1 = (2n - 1) \cos \theta \beta_{n-1}^1 - n\beta_{n-2}^1 \quad (45)$$

and the double factorial, $!!$, is a factorial where only the even terms are included.

The first order derivative of P_n^m is calculated using the following recurrence relations defined for $n > 1$ and $m > 0$

$$\frac{dP_n^0}{d\theta} = P_n^1 \quad (46)$$

$$\frac{dP_n^m}{d\theta} = n \cos \theta \beta_n^m - (n + m)\beta_{n-1}^m \quad (47)$$

The second order derivative of P_n^m is calculated using the following recurrence relations

$$\frac{d^2 P_n^0}{d\theta^2} = \frac{dP_n^1}{d\theta} = n \cos \theta \beta_n^1 - (n + 1)\beta_{n-1}^1 \quad (48)$$

$$\frac{d^2 P_n^m}{d\theta^2} = \frac{1}{2} \left[\frac{dP_n^{m+1}}{d\theta} - (n + m)(n - m + 1) \frac{dP_n^{m-1}}{d\theta} \right] \quad (49)$$

$$\frac{d^2 P_n^n}{d\theta^2} = -n \frac{dP_n^{n-1}}{d\theta} = -n \cos \theta \beta_n^{n-1} - (2n - 1)\beta_{n-1}^{n-1} \quad (50)$$

According to Petrovskaya and Vershkov [60], the derivative of $\frac{P_n^m}{\sin \theta}$ can be calculated by the following recurrence relations

$$\frac{d}{d\theta} \left(\frac{mP_n^m}{\sin \theta} \right) = m \left[\frac{1}{\sin \theta} \frac{dP_n^m}{d\theta} - \frac{\cos \theta}{\sin^2 \theta} P_n^m \right]$$

$$= \frac{1}{2} \left[(m+1) \frac{P_n^{m+1}}{\sin \theta} - (m-1)(n+m)(n-m+1) \frac{P_n^{m-1}}{\sin \theta} \right] \quad (51)$$

$$\frac{d}{d\theta} \left(\frac{m P_n^m}{\sin \theta} \right) = \frac{1}{2} \left[(m+1) \beta_n^{m+1} - (m-1)(n+m)(n-m+1) \beta_n^{m-1} \right] \quad (52)$$

For the sake of completeness, and since the spherical harmonics Y_n^m contain the term $e^{im\phi}$, we propose to use Chebyshev's recurrence relations to calculate $\cos(m\phi)$ and $\sin(m\phi)$

$$\cos(m\phi) = 2 \cos(\phi) \cos(m-1)\phi - \cos(m-2)\phi \quad (53)$$

$$\sin(m\phi) = 2 \cos(\phi) \sin(m-1)\phi - \sin(m-2)\phi \quad (54)$$

We observed that computing these terms using the above recurrence relations led to considerable savings in CPU time.

5. Vorticity diffusion in an unbounded three-dimensional flow using the redistribution method

The diffusion scheme used throughout this paper is an extension to three dimensions of the smoothed redistribution method [19,40,13], based on Shankar's redistribution scheme [12] for point vortices. In the framework of operator splitting of the vorticity equation, diffusion of vorticity is carried out as a separate step. To this end, the redistribution scheme diffuses the vorticity field as a superposition of the diffusion of all the vortex elements [19], taking advantage of the linearity of the diffusion equation. The vorticity of each vortex element i is diffused by transferring a fraction f_{ij} of its strength $\tilde{\alpha}_i$ to neighboring elements j that fall within a pre-determined distance $R_S h_d$, where $h_d = \sqrt{\nu \Delta t}$ is the diffusion length during a time step Δt and $\sqrt{4} \leq R_S \leq \sqrt{20}$ is a normalized search radius. In order to accurately model the diffusion process, these redistribution fractions are obtained by solving a system of linear equations governing the fractions f_{ij} such that the moments of the approximate and exact solution of the diffusion equation are equal up to a certain order. The number of equations is determined by the number of moments we choose to conserve and the stability of this method is ensured by enforcing the positivity of the redistribution fractions. Upon diffusing from time t to time $t + \Delta t$, the strength $\tilde{\alpha}_j$ of each vortex element j is then calculated as the sum of the received fraction from all its neighbors i ,

$$\tilde{\alpha}_j(t + \Delta t) = \sum_{i \in \mathcal{N}_j} f_{ij} \tilde{\alpha}_i(t) \quad (55)$$

where the set of neighbors \mathcal{N}_j consists of all elements within a distance of $R_S h_d$ from element j . The vorticity field is reconstructed by the superposition

$$\tilde{\omega}_\sigma(\vec{x}, t + \Delta t) = \sum_{j=1}^{N(t+\Delta t)} \tilde{\alpha}_j(t + \Delta t) \zeta_\sigma(\vec{x} - \vec{x}_j) \quad (56)$$

where N is the number of elements.

Let i be a computational element characterized by vorticity strength $\tilde{\alpha}_i$ and position \vec{x}_i . We would like to diffuse, from time t to $t + \Delta t$, the vorticity field $\tilde{\omega}_i(\vec{x}, t) = \tilde{\alpha}_i(t) \zeta_\sigma(\vec{x} - \vec{x}_i)$, associated with element i by transferring fractions f_{ij} of the element's strength $\tilde{\alpha}_i(t)$ to M neighboring elements $j \in \mathcal{N}_i$. The fractions f_{ij} are determined such that the approximated vorticity field $\sum_j f_{ij} \tilde{\alpha}_i(t) \zeta_\sigma(\vec{x} - \vec{x}_j)$ and the exact solution at time $t + \Delta t$, $\int G(\vec{x} - \vec{x}', \Delta t) \tilde{\omega}_i(\vec{x}', t) d\vec{x}'$ have the same moments, expressed in a coordinate system centered as \vec{x}_i as

$$\begin{aligned} & \int_{-\infty}^{\infty} x^m y^n z^p \sum_j f_{ij} \tilde{\alpha}_i(t) \zeta_\sigma(\vec{x} - \vec{x}_j) d\vec{x} \\ &= \int_{-\infty}^{\infty} x^m y^n z^p \left(\int_{-\infty}^{\infty} G(\vec{x} - \vec{x}', \Delta t) \tilde{\alpha}_i(t) \zeta_\sigma(\vec{x}') d\vec{x}' \right) d\vec{x}, \end{aligned} \quad (57)$$

up to order $k \geq 0$, where m, n and p are non-negative integers satisfying $0 \leq m + n + p < k$, and G is the Green's function of the diffusion equation.

For a core function of order $l = k$, after removing $\tilde{\alpha}_i(t)$ from both sides, equation (57) reduces to:

$$\begin{aligned} \sum_j f_{ij} x_j^m y_j^n z_j^p &= 0 \text{ for odd } m \text{ or } n \text{ or } p \\ &= \frac{(4\nu \Delta t)^{\frac{m+n+p}{2}} \gamma\left(\frac{m+1}{2}\right) \gamma\left(\frac{n+1}{2}\right) \gamma\left(\frac{p+1}{2}\right)}{\sqrt{\pi}^3} \text{ otherwise} \end{aligned} \quad (58)$$

where γ is the complete gamma function $\gamma(z) \equiv \int_0^\infty e^{-t} t^{z-1} dt$, especially $\gamma(1/2) = \sqrt{\pi}$.

Defining the vector $\vec{r}_{ij} = \vec{x}_j - \vec{x}_i$, and shifting coordinates to the global system of coordinates, the linear system governing f_{ij} that conserves moments up to the second order is

$$\sum_{j=1}^M f_{ij} = 1, \quad \sum_{j=1}^M f_{ij} \vec{r}_{ij} = \vec{0}, \quad (59)$$

$$\sum_{j=1}^M f_{ij} \vec{r}_{ij}^x \vec{r}_{ij}^y = 0, \quad \sum_{j=1}^M f_{ij} \vec{r}_{ij}^x \vec{r}_{ij}^z = 0, \quad \sum_{j=1}^M f_{ij} \vec{r}_{ij}^y \vec{r}_{ij}^z = 0, \quad (60)$$

$$\sum_{j=1}^M f_{ij} \vec{r}_{ij}^x \vec{r}_{ij}^x = 2\nu \Delta t, \quad \sum_{j=1}^M f_{ij} \vec{r}_{ij}^y \vec{r}_{ij}^y = 2\nu \Delta t, \quad \sum_{j=1}^M f_{ij} \vec{r}_{ij}^z \vec{r}_{ij}^z = 2\nu \Delta t \quad (61)$$

For a given order of accuracy, the redistribution equations, subject to the non-negativity constraints, are solved using the non-negative least squares (NNLS) method. If the system fails to yield non-negative fractions, new elements, selected from a set of candidates uniformly distributed on a sphere of radius $R_l h_d$, are sequentially injected until a solution is obtained, where R_l is the normalized injection radius ($R_l \simeq \sqrt{10}$). Injection of a new element is carried out in a manner that maximizes the minimum distance to the existing neighbors, which ensures some level of uniformity in the elements distribution. Introducing new elements in the diffusion process will eventually act to fill the vorticity gaps created by large strain rates which cause the particles to move away from each other and degrades the spatial resolution. This will reduce the need for remeshing since the added elements will contribute to maintaining the overlap condition. For flows with very high strain rate, one can opt to reduce the time step which in turn reduces the ratio of the advection to diffusion length scales (which scales as $O(\sqrt{\Delta t})$) leading to an improvement in the core overlap condition between neighboring particles.

6. Results and discussion

In this section, the convergence of the velocity and vortex stretching vectors, expressed as a truncated series of spherical harmonics, are first assessed by presenting the dependence of the L_2 error in the velocity and vortex stretching vector fields on the order of expansion, p . These expressions are then used to simulate the collision of two vortex rings for the following values of Reynolds numbers: $Re = 500, 1000, 1500$ and 2000 . Levels of the iso-surfaces and time dependent diagnostics, including the divergence of the vorticity, are employed to (i) compare with previous work, (ii) further assess the accuracy and convergence of the method, and (iii) to demonstrate its performance over longer times, which uncovered a third reconnection for the case $Re = 500$.

6.1. Convergence of the FMM expressions for the velocity and vortex stretching vectors

The convergence of the derived simple expressions for the velocity and vortex stretching vectors, expressed as a truncated series of spherical harmonics, is assessed as p , the order of expansion, is increased from 2 to 20. Evaluations are carried for a vortex elements distribution representing a vortex ring with a dimensionless core radius $a = 0.1$. The vorticity within the core of the ring is taken as a second-order Gaussian distribution

$$\vec{\omega}(r) = \frac{\Gamma}{2\pi a^2} \exp\left(-\frac{r^2}{2a^2}\right) \vec{e}_\theta \quad (62)$$

where \vec{e}_θ is the unit vector along the azimuthal direction, r is measured from the core center, and Γ is the circulation around the core and it is set to unity. The vorticity field, discretized using 1377744 equi-spaced elements, is approximated by

$$\vec{\omega}_\delta(\vec{x}) = \sum_i \vec{\alpha}_i \delta(\vec{x} - \vec{x}_i), \quad (63)$$

where the strength of element i is $\vec{\alpha}_i = \vec{\omega}(\vec{x}_i) dv$ and dv is the grid cell volume.

L_2 errors in the velocity and the vortex stretching vectors, calculated for both $O(N \log N)$ and $O(N)$ schemes, are plotted against the expansion order in Figs. 2 and 3, respectively. The errors, which measure the departure of the solutions predicted by the $O(N \log N)$ and $O(N)$ schemes from those obtained by direct summation, are calculated using the following L_2 norm expressions

$$L_2(\vec{v}) = \sqrt{\sum_i \|\vec{v}_f(\vec{x}_i) - \vec{v}_d(\vec{x}_i)\|^2} \quad (64)$$

$$L_2(\vec{S}) = \sqrt{\sum_i \|\vec{S}_f(\vec{x}_i) - \vec{S}_d(\vec{x}_i)\|^2} \quad (65)$$

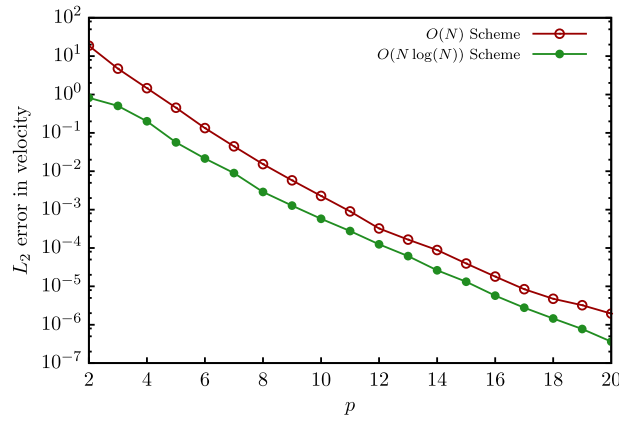


Fig. 2. L_2 norm of the velocity error vs p for $\mathcal{O}(N)$ and $\mathcal{O}(N \log N)$ schemes.

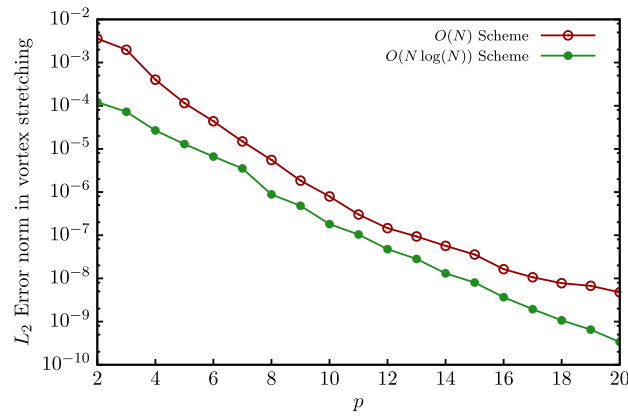


Fig. 3. L_2 norm of the vortex stretching error vs p for $\mathcal{O}(N)$ and $\mathcal{O}(N \log N)$ schemes.

where the subscripts d and f refer to the direct and fast multipole schemes respectively, and $\vec{S} = (\vec{\omega} \cdot \nabla) \vec{u}$ is the vortex stretching vector. As can be observed in Figs. 2 and 3, the solutions obtained by the fast solver converge rapidly to the direct solution as the expansion order increased, where the L_2 errors decay as C^p with C ranges between 0.41 and 0.48.

To assess the speeds of the $\mathcal{O}(N \log N)$ and $\mathcal{O}(N)$ fast solvers, the velocity and vortex stretching vectors were computed for the vorticity distribution described above. For values of p ranging from 2 to 20, the CPU execution time and the maximum relative errors in the velocity and the vortex stretching vector fields were recorded. It was found out that, for any fixed level of accuracy, the $\mathcal{O}(N)$ fast solver is always faster than the $\mathcal{O}(N \log N)$ fast solver. For example, for a maximum error of 6.23×10^{-6} in the velocity and a maximum error of 8.34×10^{-9} in the vortex stretching, the $\mathcal{O}(N)$ scheme, with $p = 12$, is 2.4 times faster than the $\mathcal{O}(N \log N)$ scheme, with $p = 9$. The ratio of the $\mathcal{O}(N)$ scheme CPU time to that of the $\mathcal{O}(N \log N)$ scheme is not constant and depends on the desired level of accuracy. In fact, for a maximum velocity error of 2×10^{-3} , the CPU time ratio is equal to 1.7. As the level of accuracy increases, the ratio increases and peaks at a value of 2.4 for a velocity error of 6.23×10^{-6} . Further increase in the level of accuracy results in a decrease in the CPU time ratio down to a value of 1.3 for a maximum velocity error of 1.9×10^{-7} , which corresponds to orders of expansion $p = 16$ and $p = 20$ for the $\mathcal{O}(N \log N)$ and $\mathcal{O}(N)$ schemes respectively.

6.2. Case study: collision of two identical axisymmetric viscous vortex rings

In this section, we present transient simulations, over a long period of time, of the collision of two vortex rings for different values of Reynolds number covering the range $Re = 500 - 2000$. We chose this problem to demonstrate the performance of the method because it has been the subject of numerous experimental and numerical studies. Kida et al. [61] numerically investigated the interaction of two identical circular viscous vortex rings using a spectral method with $64 \times 64 \times 64$ grid points. Their study explores the collision of two vortex rings at various collision angles and for initial values of Re up to 1153 over a period of time up to 60 seconds. They observed two reconnections, referred to respectively as “fusion” and “fission”, the existence of which persisted over the considered ranges of viscosity and collision angle. Moreover, the collision

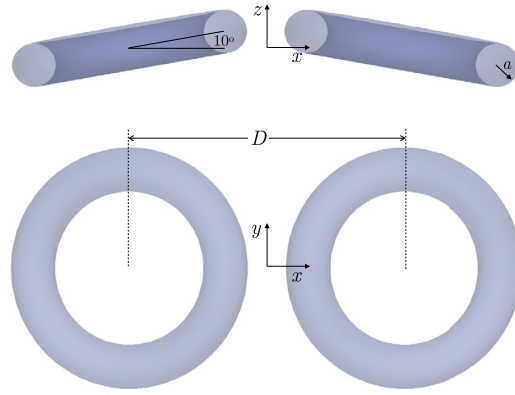


Fig. 4. Setup of the vortex rings at initial time.

of two vortex rings moving side by side has been studied experimentally by Kambe and Takao [62]. They were the first to report the occurrence of the two reconnections with the second reconnection taking place only within a narrow range of the initial linear impulse. Fohl and Turner [63] also experimentally studied the collision of two rings traveling along intersecting paths in water for a $Re \simeq 4000$. They reported the existence of a critical approach angle above which fusion and fission were always observed. Their experiments showed that while fusion always occurs below this critical angle, fission does not always follow.

In this section, we present transient simulations, over a long period of time, of the collision of two vortex rings for different values of Reynolds number covering the range $Re = 500 - 2000$. The vortex method used to numerically solve this advection-diffusion problem is completely grid-free. The operator splitting scheme employs a second Runge-Kutta time integration scheme for advection and a novel extension to three-dimensions of the redistribution method [12] for the diffusion step. In the advection step, the velocity and stretching terms are calculated using an adaptive fast multipole algorithm that combines both $\mathcal{O}(N)$ and $\mathcal{O}(N \log N)$ schemes with an order of expansion p equal to 5. The code uses the expressions developed throughout this paper and is optimized in order to reduce the calculation efforts. The elements are convected by the local velocity field and the strength vector is strained and tilted by the local stretching term using a second order Runge-Kutta method with a time step of $\Delta t = 0.1$. In the diffusion step, the 3D grid-free redistribution scheme simulates the diffusion of each particle, over a time step, by transferring non-negative fractions of its strength to its neighboring vortices in a manner that satisfies the zeroth, first, and second moments of the diffusion equation. In the process, the scheme adaptively introduces new particles in gaps introduced by large strains in the advection step. The vorticity field is approximated as

$$\vec{\omega}_\sigma(\vec{x}) = \sum_i \vec{\alpha}_i \zeta_\sigma(\vec{x} - \vec{x}_i) \quad (66)$$

where a fourth order regularizing function with smoothing radius σ is used; $\zeta_\sigma(\rho) = \frac{1}{\sigma^3} \zeta(\frac{\rho}{\sigma})$, $\zeta(\rho) = \frac{3}{8\pi} \frac{5-4\rho^6}{(1+\rho^6)^{\frac{5}{2}}}$, and $\sigma = 2.5h_0$ where $h_0 = \sqrt{10\nu\Delta t}$ is the initial elements spacing (and the injection radius).

Initially, the two vortex rings are set up as shown in Fig. 4. The rings are inclined by an angle of 10 degree towards the z axis, with their centers on the x axis.

Taking the vortex ring radius R as a characteristic length scale and the circulation around its core, Γ , as a reference circulation, the dimensionless core radius of each ring and the distance separating the centers of the two rings are chosen to be $a = 0.1$ and $D = 2.8$, respectively. The reference time is $T = R^2/\Gamma$ and the reported time is made dimensionless by dividing by T . Initially the vorticity of the ring is along the azimuthal direction and depends on r , the distance from the core center, as a second-order Gaussian distribution of Eq. (62), where \vec{e}_θ is the unit vector along the azimuthal direction. The initial vorticity distribution is represented by particles located at the cell centers of an equi-spaced radial mesh constructed for each ring. The number of mesh points increases as we move outwards to maintain the radial distance between neighboring points approximately the same equal to h_0 . Each particle is assigned with a strength vector $\vec{\alpha}_i$ equal to the value of the vorticity at particle position multiplied by the volume of the cell.

The results are presented in terms of iso-surfaces of vorticity norm and vorticity lines at several representative stages of the time evolution for $Re = 500$. These are shown in Figs. 5-6, where the levels of the iso-surfaces are 10%, 50%, and 80% of the instantaneous maximum of the vorticity norm. For $Re = 500, 1000, 1500, 2000$, we present the following time dependent diagnostics: (i) the evolution of the total kinetic energy (Fig. 14), (ii) the circulation around interacting vortex tubes during various reconnection events (Figs. 8, 9, and 10), (iii) the evolution of the error in the divergence of the vorticity (Fig. 12), (iv) growth in the number of particles as a function of time (Fig. 15), and (v) the following flow invariants (Fig. 11):

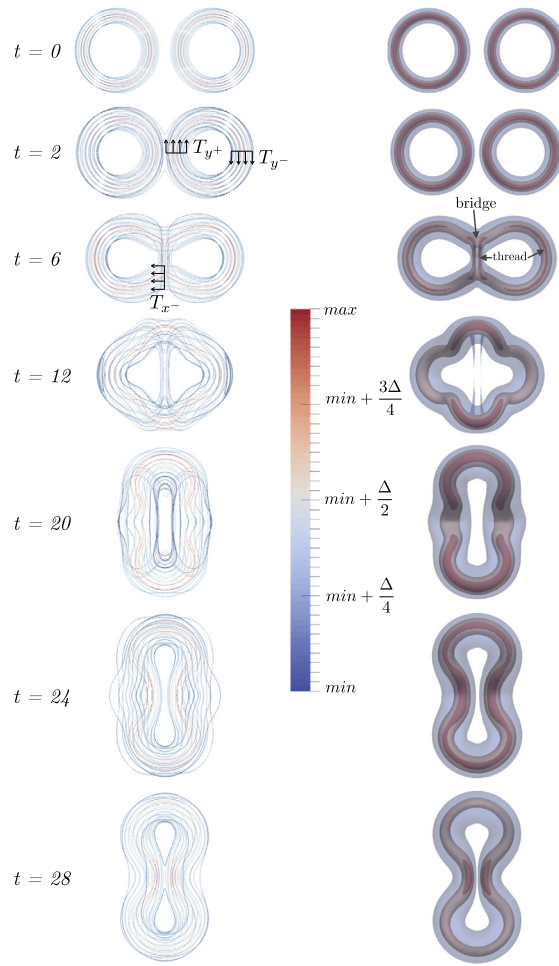


Fig. 5. Iso-surfaces of vorticity norm and a random collection of vorticity lines at several representative stages of evolution for $Re = 500$ seen from z direction. The levels of the iso-surfaces are 10%, 50%, and 80% of the instantaneous maximum of the vorticity norm. (For interpretation of the colors in the figure(s), the reader is referred to the web version of this article.)

total circulation, linear impulse, and angular impulse. We also show the impact of reducing the time step on the divergence of the vorticity for the case $Re = 2000$ (Fig. 13).

It should be noted that the degrees to which the method conserves the flow invariants and maintains the vorticity field to be divergence free are commonly used metrics to assess the convergence of the method.

6.2.1. First, second and third reconnection of the $Re = 500$ case

Figs. 5-6 show the iso-surfaces of vorticity norm and vorticity lines projected onto the (xy) plane (as seen from z direction) for the case $Re = 500$. The figures show that as the two vortex rings move along their axes due to self-induction, they undergo rotation toward the (yz) plane due to mutual induction. In effect, the rings approach each other and eventually collide at around $t = 2$. At the collision (yz) plane, viscous diffusion causes cancellation of vortex lines carrying vorticity of opposite signs, and at the same time the outermost vortex lines, that possess the lowest vorticity, start to connect forming two symmetric “bridges” of high vorticity at the back of the rings and two symmetric “threads” at the front (Fig. 6, $t = 2$), where the front and back sides are defined as in Fig. 7. Vorticity cancellation at the interaction zone is accompanied by a strong converging flow caused by vorticity away from the zone. This flow constantly brings the innermost part of the rings closer to each other which enhances the cancellation rate. In consequence, the number of reconnected vortex lines increases with time forming a single big distorted ring (Fig. 5, $t = 6$). Annihilation of vorticity in the interaction zone by viscous cross-diffusion continues to take place between the “threads” and the main distorted ring until the two “threads” disappear completely. This continues to take place until the two rings completely fuse into a single ring at $t \sim 20$ (Fig. 5). This reconnection process, referred to as vortex fusion, has been observed and described in detail by Kida et al. [61] for $Re = 577$ and 1153.

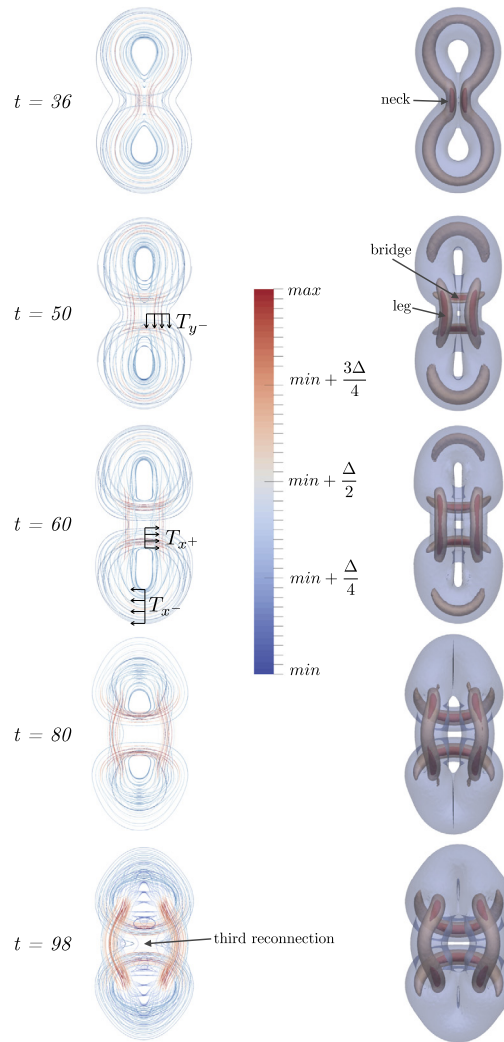


Fig. 6. Iso -surfaces of vorticity norm and a random collection of vorticity lines at several representative stages of evolution for $Re = 500$ seen from z direction. The levels of the iso-surfaces are 10%, 50%, and 80% of the instantaneous maximum of the vorticity norm.

At short times ($t < 10$ for the case $Re = 500$), the circulation is nearly constant along vortex tubes, as seen in Fig. 8. In fact, during the rings fusion process, the rate of decay of circulation $|T_{y+}|$ is balanced by an equal circulation T_{x-} gain. The circulations $|T_{y+}|$ and T_{x-} are computed respectively as vorticity integrals over the xz and yz sections shown in Fig. 5. This is clearly seen from Fig. 9 between $t = 2$ and $t = 8$ where 90% of the vortex tubes have been reconnected. These observations are in agreement with results reported by Winckelmans and Leonard [57] for $Re = 400$ and also by Kida et al. [61] for $Re = 577$ and 1153.

After the first reconnection is completed, the distorted vortex ring keeps moving in the negative z direction. Moreover, the self-induced velocity field causes stretching of the vortex tubes at the “bridges” along the y direction so that the two “bridges” rotate around the x -axis forming a plane ring that moves in the negative z direction, as shown in Fig. 7. Meanwhile the vorticity distribution also causes the outermost vortex tubes to approach each other, and the ring will have a “gourd-shaped form” [61] at around $t = 24$ as seen in Fig. 5. These tubes will continue to approach each other (narrowing of the “neck”) until they contact at around $t = 28$, triggering the second reconnection.

Similar to the first reconnection, the second reconnection takes place via “bridges”, forming at the front of the vortex ring, that connect the two tubes of opposing vorticity direction. The second reconnection is, however, slower than the first. This is because, in contrast with the first reconnection, the second reconnection cannot be maintained due to the absence of an external converging flow. This causes the second reconnection to stop early at $t = 54$, where two rings, connected by two “legs”, emerge out of the distorted ring (Fig. 6, $t = 50, 60$). At this time, only 46% of the total circulation is contained in the connecting “bridges” (Fig. 8), while the remaining uncanceled 54% are contained in the connecting “legs”. This vortex “fission” process, in which the ring seems to reverse its evolution by splitting back into two rings, has been experimentally

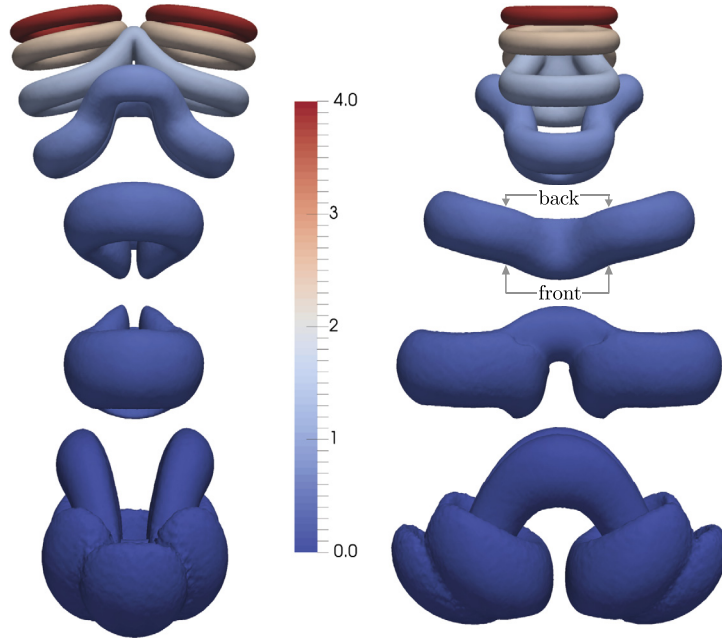


Fig. 7. Iso-surfaces of vorticity norm at several representative stages of evolution for $Re = 500$ seen from x and y directions. The level of the iso-surface is 25% of the instantaneous maximum of the vorticity norm.

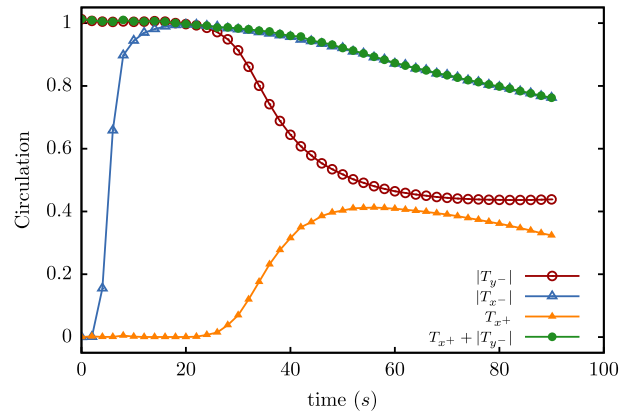


Fig. 8. Time-development of circulation around interacting vortex tubes during the first and second reconnection for $Re = 500$.

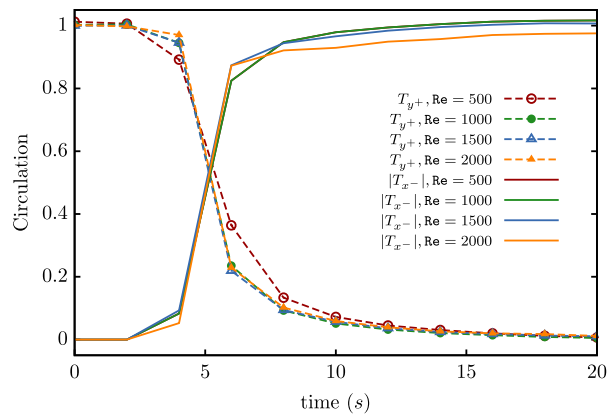


Fig. 9. Time-development of circulation around interacting vortex tubes during the first reconnection for different values of Re .

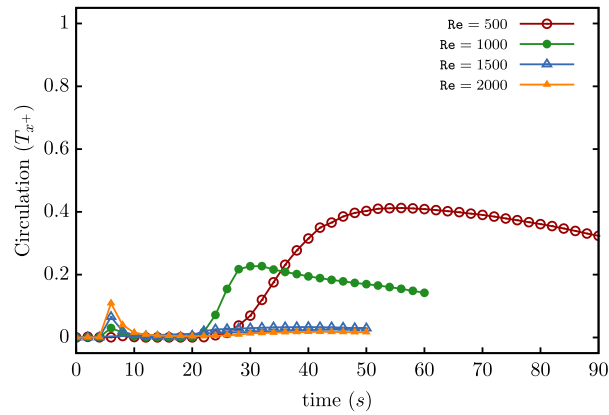


Fig. 10. Time-development of circulation around interacting vortex tubes during the second reconnection for different values of Reynolds number.

observed in [63] and numerically predicted in [61]. The reported time and speed of these processes are different than ours due to difference in the initial conditions.

Note however that the sum of the circulation passing through the “bridges” (T_{x+}) and the absolute value of that passing through the “legs” ($|T_{y-}|$) is always equal to the total circulation (which in this case is T_{x-}), as shown in Fig. 8. The circulations T_{x+} , $|T_{y-}|$, and T_{x-} are computed respectively as vorticity integrals over the yz , xz , and yz sections shown in Fig. 6. Fig. 8 also shows that T_{x-} decreases with time due to viscous cross diffusion. In fact, at around $t = 98$, the total circulation is decreased by 25%.

The vorticity in the growing “bridges” keeps increasing until it pushes the “legs” back to the positive z direction (Fig. 7). This in turn increases the “neck” curvature and the two rings formed upon the second reconnection approach each other, triggering the third reconnection that would take place at $t \simeq 98$ (Fig. 6, $t = 90$).

6.2.2. The cases $Re = 1000, 1500$, and 2000

Prior to the first reconnection, the global motion of the vortex rings, seems to be independent of the value of Re . The first reconnection starts at $t \simeq 2$ and the cancellation of vorticity in the interaction zone is complete for all cases (see Figs. 16–21 in Appendix A). We note, however, that the rate of vorticity cancellation is higher for larger values of Reynolds number, as seen in Fig. 9. This is because, despite the fact that viscosity is smaller for larger Re , the opposing vortex tubes in the interaction zone are more stretched for the larger Re case (larger vorticity), so that the net effect is a higher vorticity cancellation rate. At later times, viscosity has a bigger impact on the evolution of the vorticity field. This is manifested in a smaller approach velocity of the two rings for lower Re , resulting in a delay in the second reconnection. Fig. 10 shows that the second reconnection for $Re = 1000$ starts at $t \simeq 24$, which is ~ 4 unit time earlier than that of $Re = 500$. Moreover, the second reconnection is incomplete for higher Re , with the remaining vortices having larger circulation. In fact, for $Re = 1000$, 78% of total circulation is left uncanceled compared to 54% for $Re = 500$. For $Re = 1500$ and 2000 , the portion of the reconnected vortex tube is negligible and more than 98% of total circulation is left uncanceled. Moreover, for $Re = 1000, 1500$, and 2000 , the vorticity field leads to stretching of the vortex tubes in the x -direction which prevents any further tube reconnection. This behavior is more prominent for larger Re where the percentage of reconnected vortex tubes decreases dramatically. This is in contrast with what we observed for $Re = 500$, where the vorticity distribution pushes back the “legs” to the positive z direction, triggering a third reconnection.

These results are also in agreement with the experiments presented by Fohl and Turner [63], who reported the existence of a critical angle, equal to 16° , below which the second reconnection does not always occur. For an angle of 10° , our simulations show that the second reconnection takes place for $Re = 500$ and 1000 . However, for $Re = 1500$ and 2000 , it does not. Further studies are needed to identify the parameters which completely define the occurrence of the second reconnection.

6.2.3. Global flow invariants, vorticity divergence, and total kinetic energy

A common measure of the accuracy of vortex methods is how well they conserve the various invariants. The x , y and z components of the total vorticity are plotted against time in the first row of Fig. 11 for the different values of Re . Variation with time of the x and y components of the linear impulse, and the relative % error in its z component are plotted in the second row of Fig. 11. In addition, the x , y and z components of the angular impulse are plotted vs time in the third row of the same figure. The figures show that these quantities are conserved to within $\sim 98\%$, where the larger errors are commonly incurred for larger Re . This is attributed to the stronger inertia of the larger Re cases which results in larger strain rates that cause the particles to move away from each other which degrades the spatial resolution. Impact of inertia on the accuracy is also assessed by quantifying the departure of the divergence of the vorticity vector from zero. Fig. 12 shows that the normalized L_2 norm of the divergence of the vorticity decreases in time for all Reynolds numbers. As can be seen in the

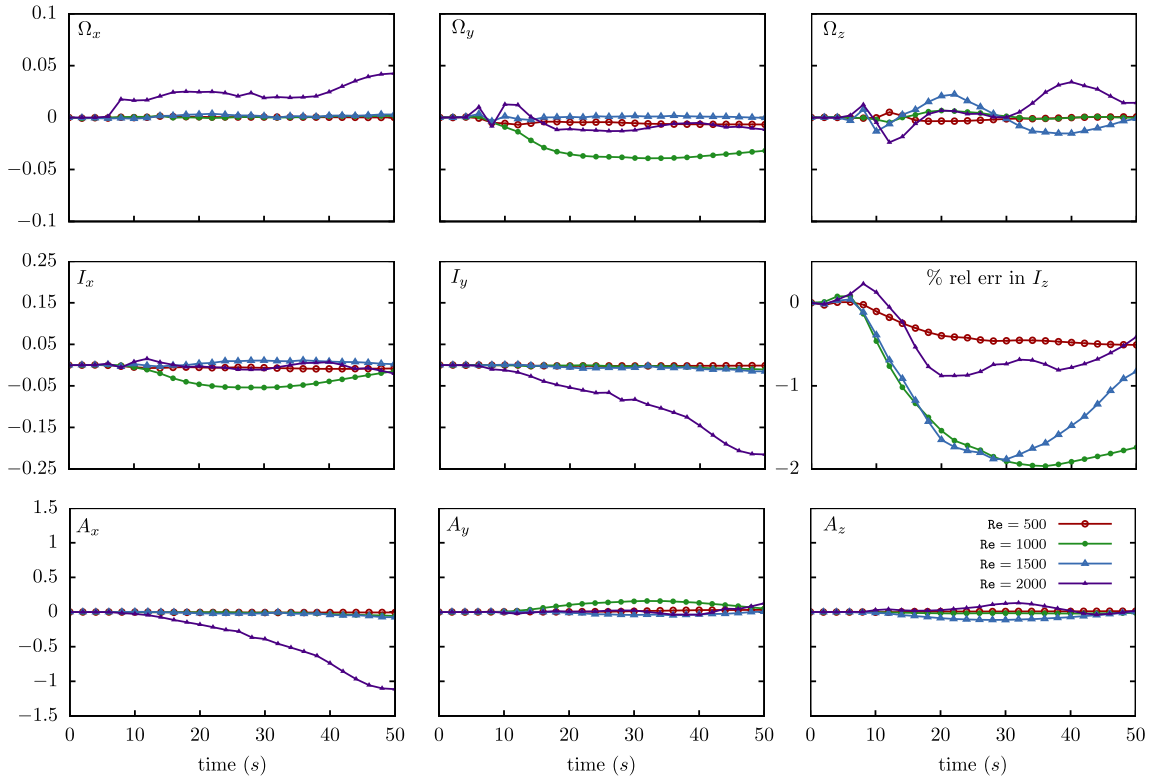


Fig. 11. The x, y, z components ($\Omega_x, \Omega_y, \Omega_z$) of the total vorticity vs time for different values of Re . The x, y components of the total linear impulse (I_x, I_y) and the % relative error in the z -component of the total linear impulse vs time for different values of Re . The x, y, z components of the total angular impulse (A_x, A_y, A_z) vs time for different values of Re .

figure, departure from the zero vorticity divergence is larger for the case with larger Re , with the peak taking place during the fusion of the two vortex rings, where vortex stretching is the characterizing mechanism. For the initial condition, the divergence was made small enough by resolving the initial vorticity field using a sufficiently large number of elements. As time increases, the vorticity divergence increases between $t = 0$ and $t = 2$ due to the dominance of inertia effects at early stages. In fact, although we didn't use any particular scheme to enforce the divergence free condition, a nearly divergence free vorticity field was maintained by the method. As time increases, although the vortex stretching tend to amplify the vorticity divergence, the diffusion process, modeled by the redistribution method, played a stabilizing role which damped the growth of the vorticity divergence throughout all the simulation and for all studied values of Reynolds number. In fact, the diffusion scheme will always contribute to filling the gaps by injecting new particles. Filling the gaps, as required by the redistribution scheme to model diffusion, acts against the large strain rates that tend to move elements farther apart. This effectively improves the overlap between neighboring elements and works towards maintaining the vorticity field to be divergence free. However, for large values of Re , and for moderate values of the time step (and default elements spacing), the strain rates are so large that the redistribution scheme will not be able, on its own, to fill the gaps properly and ensure overlap. Fig. 11 shows that this problem starts showing up at $Re = 2000$. In this case, maintaining the divergence-free vorticity field remains a challenge and the only existing cost-effective way of dealing with this challenge is re-projection. Another way, which is computationally expensive, is to reduce the time step. Fig. 13 shows that increasing the resolution of the method by reducing the time step led to a significant drop in the vorticity divergence during the fusion event. In fact, since the injection length is proportional to $\sqrt{\Delta t}$ and the advection length is proportional to Δt , decreasing the time step will eventually decrease the ratio of the advection length to injection length and will result also in an increase of the number of elements injected per unit time. These together will act to maintain the spatial resolution and dampen the variation of L_2 norm of $\nabla \cdot \vec{\omega}$. Decreasing the time step is, however, expected to help in maintaining a divergence free vorticity field only up to some point. For high Reynolds number flows, where the intense vortex stretching results in complex vorticity fields, the elements injection in the redistribution scheme will be unable to maintain the desired spatial resolution. In this case, the core overlapping condition is no longer satisfied and the numerical method rapidly loses its accuracy.

Due to viscous dissipation, the total kinetic energy decreases in time, as shown in Fig. 14. The figure also shows that the rate of decay is larger for smaller Reynolds number because of the higher viscosity.

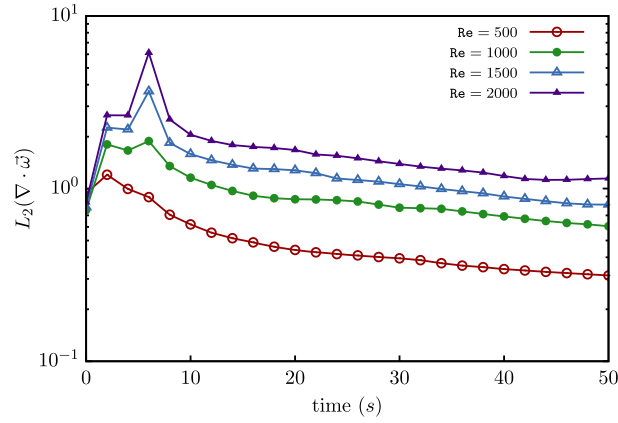


Fig. 12. L_2 norm of the vorticity divergence vs time for different values of Reynolds number. The norm is normalized by its value at $t = 0$.

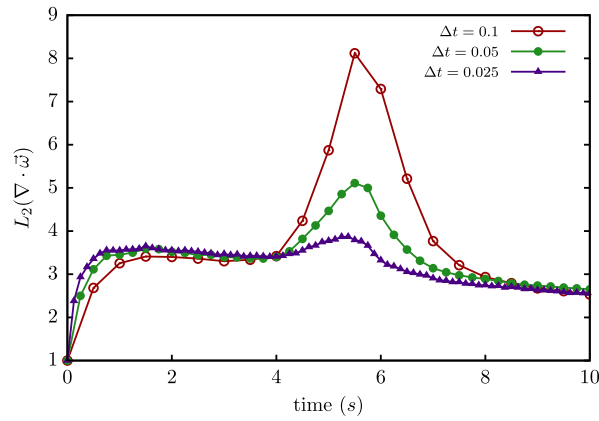


Fig. 13. L_2 norm of the vorticity divergence vs time for different values of time step. The norm is normalized by its value at $t = 0$.

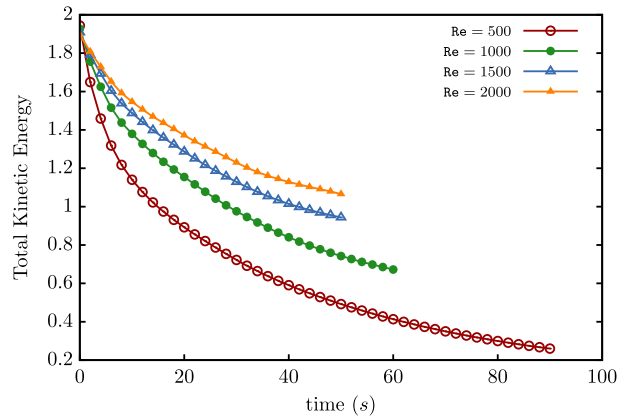


Fig. 14. Time-development of kinetic energy of the interacting vortex rings for different values of Reynolds number.

6.2.4. Computational cost

Fig. 15 shows that the growth in the number of elements with time obeys a nearly linear trend for all the cases studied. This increase is due to the fact that the redistribution scheme, used to simulate diffusion, injects new elements as neighbors of existing particles at the edge of the domain and/or in gaps created by large straining. The injection mechanism is carried out in a manner that promotes uniformity in the elements locations while conserving the various moments of the vorticity diffusion equation. Fig. 15 also shows that the number of elements increases at a higher rate for larger values of Re . This is because stronger convection creates more gaps which must be filled by the redistribution scheme. Similar trends were observed by Shankar [12] for the two dimensional flow over an impulsively started cylinder. We finally point out that

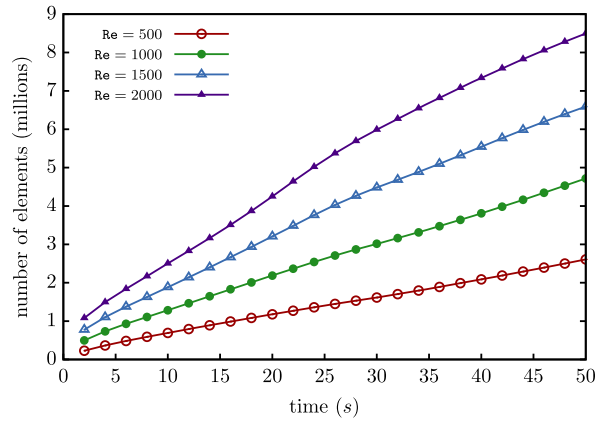


Fig. 15. Number of elements vs time for different values of Reynolds number.

optimized injection and neighbor search algorithm, in addition to parallel implementation, allows the cost of the diffusion step in terms of CPU time to be a fraction of that of the advection step.

7. Conclusions

We presented simple expressions for approximating the velocity and vortex stretching vectors induced by a far-field collection of point vortices and we proposed a set of recurrence relations to properly evaluate these expressions over the entire range of polar angle. The expressions are used by a fast solver to compute the particles velocities in the advection step of a grid-free three-dimensional vortex method. Using these expressions, we found that the solutions converge to the direct solution with the expansion order, p , as C^p , where C ranges between 0.41 and 0.48. In the diffusion step, an extension to three dimensions of the smoothed redistribution method is introduced. The diffusion scheme, along with the derived expressions, are employed to simulate the collision of two vortex rings over a long period of time. The simulations were carried out for the following values of Reynolds number: 500, 1000, 1500, 2000. The performance of the method is then assessed by comparing the evolution of the rings with previous work. The simulations showed that the first reconnection, in which the two rings fuse into a single distorted ring, persists for all considered values of Re , which is in agreement with reported experiments. The rings undergo a second reconnection which is slower than the first reconnection and where the cancellation of vorticity is incomplete. The remnant vortices have higher circulation for larger Re and the second reconnection is nearly not existing for $Re = 1500$ and 2000. These findings are also in agreement with previous experiments. The simulations uncovered a third reconnection for the case $Re = 500$, which is not reported elsewhere. The convergence of the method is also inspected in term of conserving the following flow invariants: total circulation and linear and angular impulse. All the invariants were nearly conserved (98%). Despite the fact that the method does not implement an algorithm for nullifying the non-divergent component of the computed vorticity vector, the vorticity divergence free condition was maintained for the low Reynolds number cases. This is because the redistribution scheme injects elements in gaps, created by the large strain rates, in a manner that maintains the overlap condition between neighboring elements. For large values of Re , and for moderate values of the time step, the redistribution scheme was not able to fill the gaps properly and ensure overlap which caused a noticeable non-zero divergence in the vorticity field. In this case, reducing the time step decreases the ratio of the advection to injection lengths. This effectively increases the number of injected elements per unit time which acts to maintain the spatial resolution and dampen the variation of L_2 norm of $\nabla \cdot \vec{\omega}$, as was observed during the first reconnection for the $Re = 2000$ case.

Declaration of competing interest

The authors declare that they have no known competing financial interests or personal relationships that could have appeared to influence the work reported in this paper.

Acknowledgements

This work is supported by the American University of Beirut Research Board under award number 103371.

Appendix A

Figs. 16, 18, and 20 show the time development of contours and vorticity lines, as seen from the z direction for the cases $Re = 1000$, 1500, and 2000, respectively. The corresponding iso-vorticity surfaces, as seen from the x and y directions are shown in Figs. 17, 19, and 21.

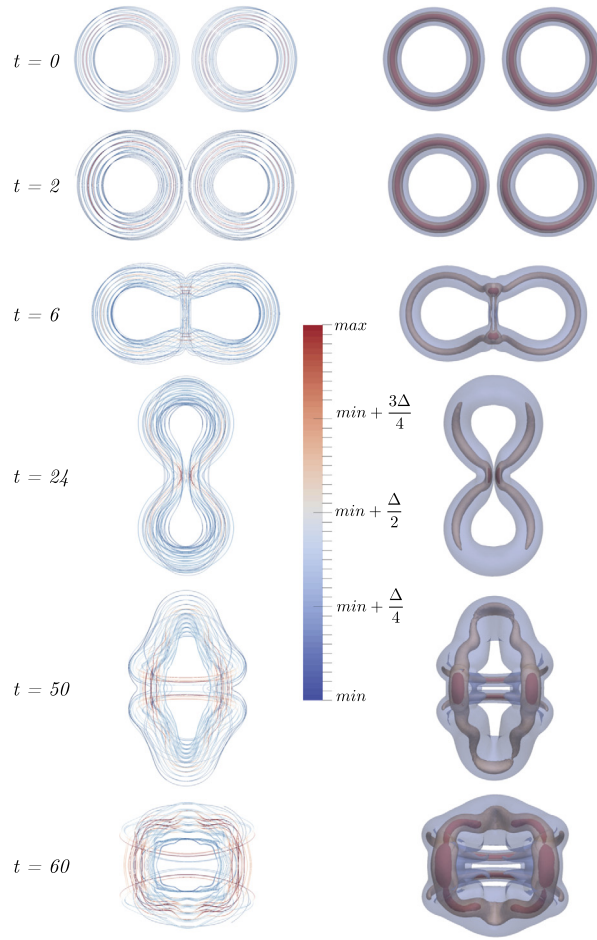


Fig. 16. Iso-surfaces of vorticity norm and a random collection of vorticity lines at several representative stages of evolution for $Re = 1000$ seen from z direction. The levels of the iso-surfaces are 10%, 50%, and 80% of the instantaneous maximum of the vorticity norm.

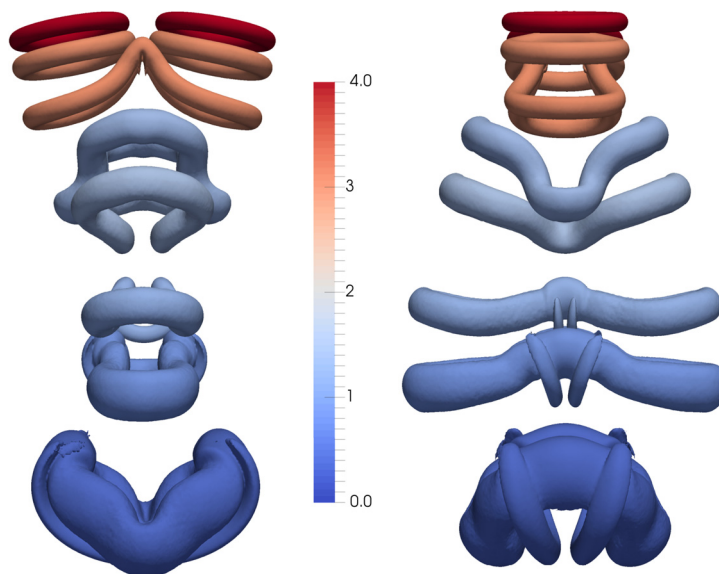


Fig. 17. Iso-surfaces of vorticity norm at several representative stages of evolution for $Re = 1000$ seen from x and y directions. The level of the iso-surface is 25% of the instantaneous maximum of the vorticity norm.

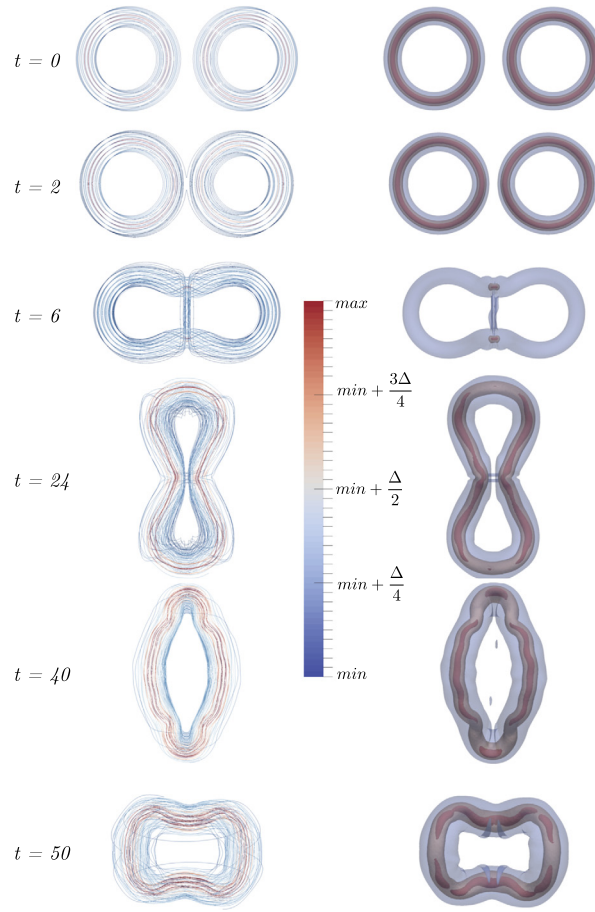


Fig. 18. Iso -surfaces of vorticity norm and a random collection of vorticity lines at several representative stages of evolution for $Re = 1500$ seen from z direction. The levels of the iso-surfaces are 10%, 50%, and 80% of the instantaneous maximum of the vorticity norm.

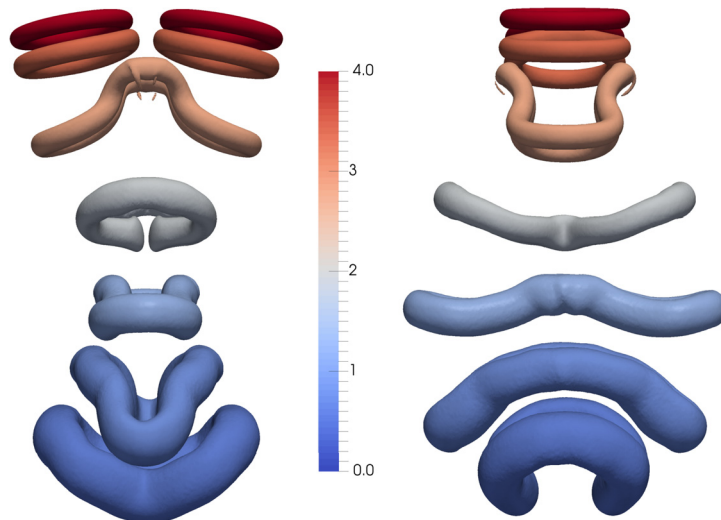


Fig. 19. Iso -surfaces of vorticity norm at several representative stages of evolution for $Re = 1500$ seen from x and y directions. The level of the iso-surface is 25% of the instantaneous maximum of the vorticity norm.

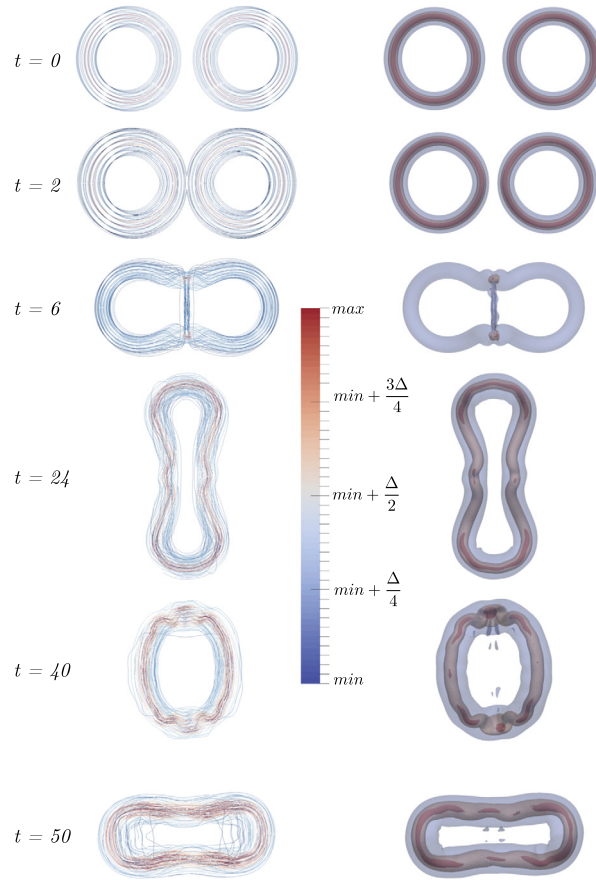


Fig. 20. Iso -surfaces of vorticity norm and a random collection of vorticity lines at several representative stages of evolution for $Re = 2000$ seen from z direction. The levels of the iso-surfaces are 10%, 50%, and 80% of the instantaneous maximum of the vorticity norm.

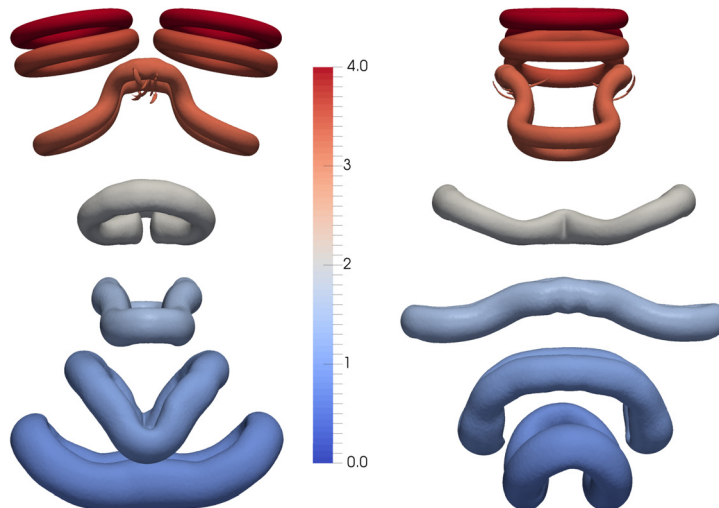


Fig. 21. Iso -surfaces of vorticity norm at several representative stages of evolution for $Re = 2000$ seen from x and y directions. The level of the iso-surface is 25% of the instantaneous maximum of the vorticity norm.

References

- [1] A.J. Chorin, Vortex methods, Pam report 593, Department of Mathematics, University of Berkeley, 1993.
- [2] A. Leonard, Vortex methods for flow simulation, *J. Comput. Phys.* 37 (1980) 289–335.
- [3] M.J. Stock, Summary of Vortex Methods Literature (a Living Document Rife with Opinion), 2007.
- [4] G.-H. Cottet, P. Koumoutsakos, *Vortex Methods: Theory and Applications*, Cambridge Univ. Press, Cambridge, UK, 2000.
- [5] G. Winckelmans, R. Cogle, L. Dufresne, R. Capart, Vortex methods and their application to trailing wake vortex simulations, *C. R. Phys.* 6 (4–5) (2005) 467–486.
- [6] R. Cogle, G. Winckelmans, G. Daeninck, Combining the vortex-in-cell and parallel fast multipole methods for efficient domain decomposition simulations, *J. Comput. Phys.* 227 (21) (2008) 9091–9120.
- [7] L. Rosenhead, The formation of vortices from a surface of discontinuity, *Proc. R. Soc. Lond. Ser. A, Contain. Pap. Math. Phys. Character* 134 (823) (1931) 170–192.
- [8] G. Birkhoff, J. Fisher, Do vortex sheets roll up?, *Rend. Circ. Mat. Palermo* 8 (1) (1959) 77–90.
- [9] A.J. Chorin, P.S. Bernard, Discretization of a vortex sheet, with an example of roll-up, *J. Comput. Phys.* 13 (3) (1973) 423–429.
- [10] A.J. Chorin, Numerical study of slightly viscous flow, *J. Fluid Mech.* 57 (1973) 785–796.
- [11] S. Mas-Gallic, P. Raviart, Particle approximation of convection-diffusion problems, Report of Univ de Paris 6, 1986.
- [12] S. Shankar, L. Dommelen, A new diffusion procedure for vortex methods, *J. Comput. Phys.* 127 (1) (1996) 88–109.
- [13] I. Lakkis, A. Ghoniem, Axisymmetric vortex method for low-mach number, diffusion-controlled combustion, *J. Comput. Phys.* 182 (2) (2003) 435–475.
- [14] J.E. Barnes, P. Hut, A hierarchical $O(n \log n)$ force calculations algorithm, *Nature* 324 (1986) 446.
- [15] L. Greengard, V. Rokhlin, A fast algorithm for particle simulations, *J. Comput. Phys.* 73 (1987) 325.
- [16] A.J. Chorin, Vortex sheed approximations of boundary layers, *J. Comput. Phys.* 27 (1978) 428–442.
- [17] P. Koumoutsakos, A. Leonard, F. Pepin, Boundary conditions for viscous vortex methods, *J. Comput. Phys.* 113 (1994) 52–61.
- [18] J. Marshall, J. Grant, Penetration of a blade into a vortex core: vorticity response and unsteady blade forces, *J. Fluid Mech.* 306 (1996) 83–109.
- [19] I. Lakkis, Grid-free vortex methods for natural convection; handling source terms and nonlinear diffusion, *Numer. Heat Transf., Part B, Fundam.* 62 (5) (2012) 370–398.
- [20] R. Krasny, Desingularization of periodic vortex sheet roll-up, *J. Comput. Phys.* 65 (2) (1986) 292–313.
- [21] R. Krasny, A study of singularity formation in a vortex sheet by the point-vortex approximation, *J. Fluid Mech.* 167 (1986) 65–93.
- [22] A. Leonard, D. Shiels, J.K. Salmon, G.S. Winckelmans, P. Ploumhans, Recent advances in high resolution vortex methods for incompressible flows, in: 13th AIAA Computational Fluid Dynamics Conf. 97, 1997, p. 2108.
- [23] P. Ploumhans, G.S. Winckelmans, Vortex methods for high-resolution simulations of viscous flow past bluff bodies of general geometry, *J. Comput. Phys.* 165 (2000) 354–406.
- [24] B. Hakizumwami, High reynolds number flow past an impulsively started circular cylinder, *Comput. Fluids* 23 (7) (1994) 895–902.
- [25] A. Cheer, Unsteady separated wake behind an impulsively started cylinder in slightly viscous flow, *J. Fluid Mech.* 201 (1989) 485–505.
- [26] O.M. Knio, A.F. Ghoniem, 3-dimensional vortex simulation of rollup and entrainment in a shear-layer, *J. Comput. Phys.* 97 (1991) 172–223.
- [27] C. Anderson, C. Greengard, On vortex methods, *SIAM J. Numer. Anal.* 22 (3) (1985) 413–440.
- [28] L. Greengard, V. Rokhlin, C. Anderson, C. Greengard, *Vortex Methods*, 1988.
- [29] O. Knio, A. Ghoniem, Vortex simulation of a three-dimensional reacting shear layer with infinite-rate kinetics, *AIAA J.* 30 (1) (1992) 105–116.
- [30] M. Soteriou, A. Ghoniem, Numerical Simulation of Unsteady Combustion Using the Transport Element Method, ESAIM: Proceedings, vol. 1, Citeseer, 1996, pp. 429–446.
- [31] A. Krishnan, A. Ghoniem, Simulation of rollup and mixing in rayleigh-taylor flow using the transport-element method, *J. Comput. Phys.* 99 (1992) 1–27.
- [32] I. Lakkis, A.F. Ghoniem, Lagrangian simulation of fire plumes, in: 7th AIAA/ASME Joint Thermo and Heat Transf. Conf. 1, 1998, pp. 215–226.
- [33] A.F. Ghoniem, I. Lakkis, M. Soteriou, Numerical simulation of the dynamics of large fire plumes and the phenomenon of puffing, in: 26th Symp. (Int.) Comb., The Combustion Institute, 1996, pp. 1531–1539.
- [34] J.D. Eldredge, T. Colonius, A. Leonard, A vortex particle method for two-dimensional compressible flow, *J. Comput. Phys.* 179 (2) (2002) 371–399.
- [35] F. Schlegel, D. Wee, A. Ghoniem, A fast 3d particle method for the simulation of buoyant flow, *J. Comput. Phys.* 227 (21) (2008) 9063–9090.
- [36] J. Ray, H. Najm, R. Milne, K. Devine, S. Kempka, Triple flame structure and dynamics at the stabilization point of an unsteady lifted jet diffusion flame, *Proc. Combust. Inst.* 28 (1) (2000) 219–226.
- [37] H. Najm, R. Milne, K. Devine, S. Kempka, A coupled lagrangian-eulerian scheme for reacting flow modeling, *ESAIM Proc.* 7 (1999) 304–313, edpsciences.org.
- [38] I. Lakkis, A. Ghoniem, Grid-free simulation of radiative transport in a participating medium, *ESAIM Proc.* 7 (1999) 234–246, edpsciences.org.
- [39] I. Lakkis, A. Ghoniem, Grid-free simulation of a reacting radiating fuel ring, in: AIAA, Aerospace Sciences Meeting and Exhibit, 38 th, Reno, NV, 2000.
- [40] I. Lakkis, A. Ghoniem, A high resolution spatially adaptive vortex method for separating flows. part i: Two-dimensional domains, *J. Comput. Phys.* 228 (2) (2009) 491–515.
- [41] M. Ould-Salihi, G. Cottet, M. El Hamraoui, Blending finite-difference and vortex methods for incompressible flow computations, *SIAM J. Sci. Comput.* 22 (5) (2001) 1655–1674.
- [42] E. Stein, R. De Borst, T.J. Hughes, in: *Encyclopedia of Computational Mechanics*, 2004.
- [43] G. Winckelmans, U.C.D. Louvain, J.K. Salmon, A. Leonard, B. Jodoin, Application of Fast Parallel and Sequential Tree Codes to Computing Three-Dimensional Flows with the Vortex Element and Boundary Element Methods, 1996.
- [44] G. Pedrizzetti, Insight into singular vortex flows, *Fluid Dyn. Res.* 10 (2) (1992) 101.
- [45] J. Christiansen, Numerical simulation of hydrodynamics by the method of point vortices, *J. Comput. Phys.* 13 (3) (1973) 363–379.
- [46] G. Cottet, B. Michaux, S. Ossia, G. VanderLinden, A comparison of spectral and vortex methods in three-dimensional incompressible flows, *J. Comput. Phys.* 175 (2) (2002) 702–712.
- [47] P. Chatelain, P. Koumoutsakos, A fourier-based elliptic solver for vortical flows with periodic and unbounded directions, *J. Comput. Phys.* 229 (7) (2010) 2425–2431.
- [48] R. Yokota, An FMM based on dual tree traversal for many-core architectures, CoRR, arXiv:1209.3516 [abs], 2012.
- [49] J.K. Salmon, M.S. Warren, Skeletons from the treecode closet, *J. Comput. Phys.* 111 (1) (1994) 136–155.
- [50] R. Yokota, L. Barba, Hierarchical n-body simulations with autotuning for heterogeneous systems, *Comput. Sci. Eng.* 14 (3) (2012) 30–39.
- [51] P. Ploumhans, G.S. Winckelmans, J.K. Salmon, A. Leonard, M.S. Warren, Vortex methods for direct numerical simulation of three-dimensional bluff body flows: application to the sphere at $Re = 300, 500$, and 1000 , *J. Comput. Phys.* 178 (2002) 427–463.
- [52] R. Yokota, T.K. Sheel, S. Obi, Calculation of isotropic turbulence using a pure lagrangian vortex method, *J. Comput. Phys.* 226 (2) (2007) 1589–1606.
- [53] R. Yokota, T. Narumi, R. Sakamaki, S. Kameoka, S. Obi, K. Yasuoka, Fast multipole methods on a cluster of gpus for the meshless simulation of turbulence, *Comput. Phys. Commun.* 180 (11) (2009) 2066–2078.
- [54] R. Yokota, L. Barba, Fmm-based vortex method for simulation of isotropic turbulence on gpus, compared with a spectral method, *Comput. Fluids* 80 (2013) 17–27.

- [55] T. Berdowski, J. Walther, C. Ferreira, F. Meng, Derivation and analysis of the analytical velocity and vortex stretching expressions for an $O(n \log n)$ -fmm, *J. Phys. Conf. Ser.* 753 (2016) 082023, IOP Publishing.
- [56] J. Beale, A. Majda, High order accurate vortex methods with explicit velocity kernels, *J. Comput. Phys.* 58 (2) (1985) 188–208.
- [57] G. Winckelmans, A. Leonard, Contributions to vortex particle methods for the computation of three-dimensional incompressible unsteady flows, *J. Comput. Phys.* 109 (2) (1993) 247–273.
- [58] R. Beatson, L. Greengard, A short course on fast multipole methods, in: *Wavelets, Multilevel Methods and Elliptic PDEs* 1, 1997, pp. 1–37.
- [59] W. Bosch, On the computation of derivatives of legendre functions, *Phys. Chem. Earth, Part A, Solid Earth Geod.* 25 (9–11) (2000) 655–659.
- [60] M. Petrovskaya, A. Vershkov, Non-singular expressions for the gravity gradients in the local north-oriented and orbital reference frames, *J. Geod.* 80 (3) (2006) 117–127.
- [61] S. Kida, M. Takaoka, F. Hussain, Collision of two vortex rings, *J. Fluid Mech.* 230 (1991) 583–646.
- [62] T. Kambe, T. Takao, Motion of distorted vortex rings, *J. Phys. Soc. Jpn.* 31 (2) (1971) 591–599.
- [63] T. Fohl, J. Turner, Colliding vortex rings, *Phys. Fluids* 18 (4) (1975) 433–436.